Characterization of the astrophysical diffuse neutrino flux using starting track events in IceCube

R. Abbasi,[17] M. Ackermann,[64] J. Adams,[18] S. K. Agarwalla,[40,*] J. A. Aguilar,[12] M. Ahlers,[22] J. M. Alameddine,[23] N. M. Amin,[44] K. Andeen,[42] G. Anton,[26] C. Argüelles,[14] Y. Ashida,[53] S. Athanasiadou,[64] L. Ausborm,[1] S. N. Axani,[44] X. Bai,[50] A. Balagopal,[40] M. Baricevic,[40] S. W. Barwick,[30] S. Bash,[27] V. Basu,[40] R. Bay,[8] J. J. Beatty,[20,21] J. Becker Tjus,[11,†] J. Beise,[62] C. Bellenghi,[27] C. Benning,[1] S. BenZvi,[52] D. Berley,[19] E. Bernardini,[48] D. Z. Besson,[36] E. Blaufuss,[19] S. Blot,[64] F. Bontempo,[31] J. Y. Book,[14] C. Boscolo Meneguolo,[48] S. Böser,[41] O. Botner,[62] J. Böttcher,[1] J. Braun,[40] B. Brinson,[6] J. Brostean-Kaiser,[64] L. Brusa,[1] R. T. Burley,[2] R. S. Busse,[43] D. Butterfield,[40] M. A. Campana,[49] I. Caracas,[41] K. Carloni,[14] J. Carpio,[34,35] S. Chattopadhyay,[40,*] N. Chau,[12] Z. Chen,[56] D. Chirkin,[40] S. Choi,[57] B. A. Clark,[19] A. Coleman,[62] G. H. Collin,[15] A. Connolly,[20,21] J. M. Conrad,[15] P. Coppin,[13] R. Corley,[53] P. Correa,[13] D. F. Cowen,[60,61] P. Dave,[6] C. De Clercq,[13] J. J. DeLaunay,[59] D. Delgado,[14] S. Deng,[1] K. Deoskar,[55] A. Desai,[40] P. Desiati,[40] K. D. de Vries,[13] G. de Wasseige,[37] T. DeYoung,[24] A. Diaz,[15] J. C. Díaz-Vélez,[40] M. Dittmer,[43] A. Domi,[26] L. Draper,[53] H. Dujmovic,[40] M. A. DuVernois,[40] T. Ehrhardt,[41] L. Eidenschink,[27] A. Eimer,[26] P. Eller,[27] E. Ellinger,[63] S. El Mentawi,[1] D. Elsässer,[23] R. Engel,[31,32] H. Erpenbeck,[40] J. Evans,[19] P. A. Evenson,[44] K. L. Fan,[19] K. Fang,[40] K. Farrag,[16] A. R. Fazely,[7] A. Fedynitch,[58] N. Feigl,[10] S. Fiedlschuster,[26] C. Finley,[55] L. Fischer,[64] D. Fox,[60] A. Franckowiak,[11] P. Fürst,[1] J. Gallagher,[39] E. Ganster,[1] A. Garcia,[14] E. Genton,[37] L. Gerhardt,[9] A. Ghadimi,[59] C. Girard-Carillo,[41] C. Glaser,[62] T. Glüsenkamp,[26,62] J. G. Gonzalez,[44] S. Goswami,[34,35] A. Granados,[24] D. Grant,[24] S. J. Gray,[19] O. Gries,[1] S. Griffin,[40] S. Griswold,[52] K. M. Groth,[22] C. Günther,[1] P. Gutjahr,[23] C. Ha,[54] C. Haack,[26] A. Hallgren,[62] R. Halliday,[24] L. Halve,[1] F. Halzen,[40] H. Hamdaoui,[56] M. Ha Minh,[27] M. Handt,[1] K. Hanson,[40] J. Hardin,[15] A. A. Harnisch,[24] P. Hatch,[33] A. Haungs,[31] J. Häußler,[1] K. Helbing,[63] J. Hellrung,[11] J. Hermannsgabner,[1] L. Heuermann,[1] N. Heyer,[62] S. Hickford,[63] A. Hidvegi,[55] C. Hill,[16] G. C. Hill,[2] K. D. Hoffman,[19] S. Hori,[40] K. Hoshina,[40,‡] M. Hostert,[14] W. Hou,[31] T. Huber,[31] K. Hultqvist,[55] M. Hünnefeld,[23] R. Hussain,[40] K. Hymon,[23] A. Ishihara,[16] W. Iwakiri,[16] M. Jacquart,[40] O. Janik,[26] M. Jansson,[55] G. S. Japaridze,[5] M. Jeong,[53] M. Jin,[14] B. J. P. Jones,[4] N. Kamp,[14] D. Kang,[31] W. Kang,[57] X. Kang,[49] A. Kappes,[43] D. Kappesser,[41] L. Kardum,[23] T. Karg,[64] M. Karl,[27] A. Karle,[40] A. Katil,[25] U. Katz,[26] M. Kauer,[40] J. L. Kelley,[40] M. Khanal,[53] A. Khatee Zathul,[40] A. Kheirandish,[34,35] J. Kiryluk,[56] S. R. Klein,[8,9] A. Kochocki,[24] R. Koirala,[44] H. Kolanoski,[10] T. Kontrimas,[27] L. Köpke,[41] C. Kopper,[26] D. J. Koskinen,[22] P. Koundal,[44] M. Kovacevich,[49] M. Kowalski,[10,64] T. Kozynets,[22] J. Krishnamoorthi,[40,*] K. Kruiswijk,[37] E. Krupczak,[24] A. Kumar,[64] E. Kun,[11] N. Kurahashi,[49] N. Lad,[64] C. Lagunas Gualda,[64] M. Lamoureux,[37] M. J. Larson,[19] S. Latseva,[1] F. Lauber,[63] J. P. Lazar,[37] J. W. Lee,[57] K. Leonard DeHolton,[60,61] A. Leszczyńska,[44] J. Liao,[6] M. Lincetto,[11] M. Liubarska,[25] E. Lohfink,[41] C. Love,[49] C. J. Lozano Mariscal,[43] L. Lu,[40] F. Lucarelli,[28] W. Luszczak,[20,21] Y. Lyu,[8,9] J. Madsen,[40] E. Magnus,[13] K. B. M. Mahn,[24] Y. Makino,[40] E. Manao,[27] S. Mancina,[40,48] W. Marie Sainte,[40] I. C. Mariş,[12] S. Marka,[46] Z. Marka,[46] M. Marsee,[59] I. Martinez-Soler,[14] R. Maruyama,[45] F. Mayhew,[24] T. McElroy,[25] F. McNally,[38] J. V. Mead,[22] K. Meagher,[40] S. Mechbal,[64] A. Medina,[21] M. Meier,[16] Y. Merckx,[13] L. Merten,[11] J. Micallef,[24] J. Mitchell,[7] T. Montaruli,[28] R. W. Moore,[25] Y. Morii,[16] R. Morse,[40] M. Moulai,[40] T. Mukherjee,[31] R. Naab,[64] R. Nagai,[16] M. Nakos,[40] U. Naumann,[63] J. Necker,[64] A. Negi,[4] M. Neumann,[43] H. Niederhausen,[24] M. U. Nisa,[24] A. Noell,[1] A. Novikov,[44] S. C. Nowicki,[24] A. Obertacke Pollmann,[16] V. O'Dell,[40] B. Oeyen,[29] A. Olivas,[19] R. Orsoe,[27] J. Osborn,[40] E. O'Sullivan,[62] H. Pandya,[44] N. Park,[33] G. K. Parker,[4] E. N. Paudel,[44] L. Paul,[50] C. Pérez de los Heros,[62] T. Pernice,[64] J. Peterson,[40] S. Philippen,[1] A. Pizzuto,[40] M. Plum,[50] A. Pontén,[62] Y. Popovych,[41] M. Prado Rodriguez,[40] B. Pries,[24] R. Procter-Murphy,[19] G. T. Przybylski,[9] C. Raab,[37] J. Rack-Helleis,[41] K. Rawlins,[3] Z. Rechav,[40] A. Rehman,[44] P. Reichherzer,[11] E. Resconi,[27] S. Reusch,[64] W. Rhode,[23] B. Riedel,[40] A. Rifaie,[1] E. J. Roberts,[2] S. Robertson,[8,9] S. Rodan,[57] G. Roellinghoff,[57] M. Rongen,[26] A. Rosted,[16] C. Rott,[53,57] T. Ruhe,[23] L. Ruohan,[27] D. Ryckbosch,[29] I. Safa,[40] J. Saffer,[32] D. Salazar-Gallegos,[24] P. Sampathkumar,[31] A. Sandrock,[63] M. Santander,[59] S. Sarkar,[25] S. Sarkar,[47] J. Savelberg,[1] P. Savina,[40] P. Schaile,[27] M. Schaufel,[1] H. Schieler,[31] S. Schindler,[26] B. Schlüter,[43] F. Schlüter,[12] N. Schmeisser,[63] T. Schmidt,[19] J. Schneider,[26] F. G. Schröder,[31,44] L. Schumacher,[26] S. Sclafani,[19] D. Seckel,[44] M. Seikh,[36] M. Seo,[57] S. Seunarine,[51] P. Sevle Myhr,[37] R. Shah,[49] S. Shefali,[32] N. Shimizu,[16] M. Silva,[40] B. Skrzypek,[8] B. Smithers,[4] R. Snihur,[40] J. Soedingrekso,[23] A. Søgaard,[22] D. Soldin,[53] P. Soldin,[1] G. Sommani,[11] C. Spannfellner,[27] G. M. Spiczak,[51] C. Spiering,[64] M. Stamatikos,[21] T. Stanev,[44] T. Stezelberger,[9] T. Stürwald,[63] T. Stuttard,[22] G. W. Sullivan,[19] I. Taboada,[6] S. Ter-Antonyan,[7] A. Terliuk,[27] M. Thiesmeyer,[1] W. G. Thompson,[14] J. Thwaites,[40] S. Tilav,[44] K. Tollefson,[24] C. Tönnis,[57] S. Toscano,[12] D. Tosi,[40] A. Trettin,[64] R. Turcotte,[31] J. P. Twagirayezu,[24] M. A. Unland Elorrieta,[43] A. K. Upadhyay,[40,*] K. Upshaw,[7] A. Vaidyanathan,[42] N. Valtonen-Mattila,[62] J. Vandenbroucke,[40] N. van Eijndhoven,[13] D. Vannerom,[15] J. van Santen,[64] J. Vara,[43] J. Veitch-Michaelis,[40] M. Venugopal,[31] M. Vereecken,[37] S. Verpoest,[44] D. Veske,[46] A. Vijai,[19] C. Walck,[55] A. Wang,[6] C. Weaver,[24] P. Weigel,[15] A. Weindl,[31] J. Weldert,[60,61] A. Y. Wen,[14] C. Wendt,[40] J. Werthebach,[23] M. Weyrauch,[31] N. Whitehorn,[24] C. H. Wiebusch,[1]

D. R. Williams,[59] L. Witthaus,[23] A. Wolf,[1] M. Wolf,[27] G. Wrede,[26] X. W. Xu,[7] J. P. Yanez,[25] E. Yildizci,[40] S. Yoshida,[16] R. Young,[36] S. Yu,[53] T. Yuan,[40] Z. Zhang,[56] P. Zhelnin,[14] P. Zilberman,[40] and M. Zimmerman[40]

(IceCube Collaboration)

[1]*III. Physikalisches Institut, RWTH Aachen University, D-52056 Aachen, Germany*
[2]*Department of Physics, University of Adelaide, Adelaide 5005, Australia*
[3]*Department of Physics and Astronomy, University of Alaska Anchorage,*
3211 Providence Dr., Anchorage, Alaska 99508, USA
[4]*Department of Physics, University of Texas at Arlington, 502 Yates St.,*
Science Hall Rm 108, Box 19059, Arlington, Texas 76019, USA
[5]*CTSPS, Clark-Atlanta University, Atlanta, Georgia 30314, USA*
[6]*School of Physics and Center for Relativistic Astrophysics, Georgia Institute of Technology,*
Atlanta, Georgia 30332, USA
[7]*Department of Physics, Southern University, Baton Rouge, Los Angeles 70813, USA*
[8]*Department of Physics, University of California, Berkeley, California 94720, USA*
[9]*Lawrence Berkeley National Laboratory, Berkeley, California 94720, USA*
[10]*Institut für Physik, Humboldt-Universität zu Berlin, D-12489 Berlin, Germany*
[11]*Fakultät für Physik & Astronomie, Ruhr-Universität Bochum, D-44780 Bochum, Germany*
[12]*Université Libre de Bruxelles, Science Faculty CP230, B-1050 Brussels, Belgium*
[13]*Vrije Universiteit Brussel (VUB), Dienst ELEM, B-1050 Brussels, Belgium*
[14]*Department of Physics and Laboratory for Particle Physics and Cosmology, Harvard University,*
Cambridge, Massachusetts 02138, USA
[15]*Department of Physics, Massachusetts Institute of Technology, Cambridge, Massachusetts 02139, USA*
[16]*Department of Physics and The International Center for Hadron Astrophysics,*
Chiba University, Chiba 263-8522, Japan
[17]*Department of Physics, Loyola University Chicago, Chicago, Illinois 60660, USA*
[18]*Department of Physics and Astronomy, University of Canterbury,*
Private Bag 4800, Christchurch, New Zealand
[19]*Department of Physics, University of Maryland, College Park, Maryland 20742, USA*
[20]*Department of Astronomy, Ohio State University, Columbus, Ohio 43210, USA*
[21]*Department of Physics and Center for Cosmology and Astro-Particle Physics,*
Ohio State University, Columbus, Ohio 43210, USA
[22]*Niels Bohr Institute, University of Copenhagen, DK-2100 Copenhagen, Denmark*
[23]*Department of Physics, TU Dortmund University, D-44221 Dortmund, Germany*
[24]*Department of Physics and Astronomy, MichiGeorgian State University,*
East Lansing, Michigan 48824, USA
[25]*Department of Physics, University of Alberta, Edmonton, Alberta, T6G 2E1, Canada*
[26]*Erlangen Centre for Astroparticle Physics, Friedrich-Alexander-Universität Erlangen-Nürnberg,*
D-91058 Erlangen, Germany
[27]*Physik-department, Technische Universität München, D-85748 Garching, Germany*
[28]*Département de physique nucléaire et corpusculaire, Université de Genève,*
CH-1211 Genève, Switzerland
[29]*Department of Physics and Astronomy, University of Gent, B-9000 Gent, Belgium*
[30]*Department of Physics and Astronomy, University of California, Irvine, California 92697, USA*
[31]*Karlsruhe Institute of Technology, Institute for Astroparticle Physics, D-76021 Karlsruhe, Germany*
[32]*Karlsruhe Institute of Technology, Institute of Experimental Particle Physics,*
D-76021 Karlsruhe, Germany
[33]*Department of Physics, Engineering Physics, and Astronomy, Queen's University,*
Kingston, ON K7L 3N6, Canada
[34]*Department of Physics & Astronomy, University of Nevada, Las Vegas, Nevada 89154, USA*
[35]*Nevada Center for Astrophysics, University of Nevada, Las Vegas, Nevada 89154, USA*
[36]*Department of Physics and Astronomy, University of Kansas, Lawrence, Kansas 66045, USA*
[37]*Centre for Cosmology, Particle Physics and Phenomenology - CP3, Université catholique de Louvain,*
Louvain-la-Neuve, Belgium
[38]*Department of Physics, Mercer University, Macon, Georgia 31207-0001, USA*
[39]*Department of Astronomy, University of Wisconsin—Madison, Madison, Wisconsin 53706, USA*
[40]*Department of Physics and Wisconsin IceCube Particle Astrophysics Center,*
University of Wisconsin—Madison, Madison, Wisconsin 53706, USA
[41]*Institute of Physics, University of Mainz, Staudinger Weg 7, D-55099 Mainz, Germany*

^{42}*Department of Physics, Marquette University, Milwaukee, Wisconsin 53201, USA*

^{43}*Institut für Kernphysik, Westfälische Wilhelms-Universität Münster, D-48149 Münster, Germany*

^{44}*Bartol Research Institute and Department of Physics and Astronomy, University of Delaware,
Newark, Delaware 19716, USA*

^{45}*Department of Physics, Yale University, New Haven, Connecticut 06520, USA*

^{46}*Columbia Astrophysics and Nevis Laboratories, Columbia University, New York, New York 10027, USA*

^{47}*Department of Physics, University of Oxford, Parks Road, Oxford OX1 3PU, United Kingdom*

^{48}*Dipartimento di Fisica e Astronomia Galileo Galilei, Università Degli Studi di Padova,
I-35122 Padova PD, Italy*

^{49}*Department of Physics, Drexel University, 3141 Chestnut Street, Philadelphia, Pennsylvania 19104, USA*

^{50}*Physics Department, South Dakota School of Mines and Technology,
Rapid City, South Dakota 57701, USA*

^{51}*Department of Physics, University of Wisconsin, River Falls, Wisconsin 54022, USA*

^{52}*Department of Physics and Astronomy, University of Rochester, Rochester, New York 14627, USA*

^{53}*Department of Physics and Astronomy, University of Utah, Salt Lake City, Utah 84112, USA*

^{54}*Department of Physics, Chung-Ang University, Seoul 06974, Republic of Korea*

^{55}*Oskar Klein Centre and Department of Physics, Stockholm University, SE-10691 Stockholm, Sweden*

^{56}*Department of Physics and Astronomy, Stony Brook University, Stony Brook, New York 11794-3800, USA*

^{57}*Department of Physics, Sungkyunkwan University, Suwon 16419, Republic of Korea*

^{58}*Institute of Physics, Academia Sinica, Taipei, 11529, Taiwan*

^{59}*Department of Physics and Astronomy, University of Alabama, Tuscaloosa, Alabama 35487, USA*

^{60}*Department of Astronomy and Astrophysics, Pennsylvania State University,
University Park, Pennsylvania 16802, USA*

^{61}*Department of Physics, Pennsylvania State University, University Park, Pennsylvania 16802, USA*

^{62}*Department of Physics and Astronomy, Uppsala University, Box 516, SE-75120 Uppsala, Sweden*

^{63}*Department of Physics, University of Wuppertal, D-42119 Wuppertal, Germany*

^{64}*Deutsches Elektronen-Synchrotron DESY, Platanenallee 6, D-15738 Zeuthen, Germany*

A measurement of the diffuse astrophysical neutrino spectrum is presented using IceCube data collected from 2011–2022 (10.3 years). We developed novel detection techniques to search for events with a contained vertex and exiting track induced by muon neutrinos undergoing a charged-current interaction. Searching for these starting track events allows us to not only more effectively reject atmospheric muons but also atmospheric neutrino backgrounds in the southern sky, opening a new window to the sub-100 TeV astrophysical neutrino sky. The event selection is constructed using a dynamic starting track veto and machine learning algorithms. We use this data to measure the astrophysical diffuse flux as a single power law flux (SPL) with a best-fit spectral index of $\gamma = 2.58^{+0.10}_{-0.09}$ and per-flavor normalization of $\phi^{\mathrm{Astro}}_{\mathrm{per\text{-}flavor}} = 1.68^{+0.19}_{-0.22} \times 10^{-18} \times \mathrm{GeV}^{-1}\,\mathrm{cm}^{-2}\,\mathrm{s}^{-1}\,\mathrm{sr}^{-1}$ (at 100 TeV). The sensitive energy range for this dataset is 3–550 TeV under the SPL assumption. This data was also used to measure the flux under a broken power law, however we did not find any evidence of a low energy cutoff.

I. INTRODUCTION

High energy astrophysical neutrinos were discovered by IceCube in 2013 [1–3]; since then, there have been many efforts to understand the production mechanisms by which these high energy neutrinos are created. Energetic neutrinos are decay products, and the neutrino flux points directly to the processes that created it [4]. In particular, we know there are extremely energetic accelerators which drive cosmic rays to very high energies via processes such as Fermi acceleration [5–7].

It is expected that some cosmic rays will interact with hadronic matter or the photon flux near their source. Charged pions $(\pi^{\pm})$ and kaons $(K^{\pm})$, produced in these interactions decay into neutrinos and muons $(\pi^{\pm} \to \nu_{\mu}(\bar{\nu}_{\mu}) + \mu^{\pm})$, with the muons subsequently decaying into electrons and

---

*Also at Institute of Physics, Sachivalaya Marg, Sainik School Post, Bhubaneswar 751005, India.

†Also at Department of Space, Earth and Environment, Chalmers University of Technology, 412 96 Gothenburg, Sweden.

‡Also at Earthquake Research Institute, University of Tokyo, Bunkyo, Tokyo 113-0032, Japan.

neutrinos $[\mu^\pm \to e^\pm + \bar{\nu}_e(\nu_e) + \nu_\mu(\bar{\nu}_\mu)]$. In this scenario, the neutrino flavor ratio at the source is $\nu_\mu : \nu_e : \nu_\tau = 2:1:0$ with oscillations converting this ratio to approximately $1:1:1$ [8] at Earth, although there are alternative scenarios which predict other ratios [9].

In this paper, we present a measurement of the diffuse astrophysical neutrino flux using novel classification techniques and methods to reconstruct event observables. The event selection and techniques described in this paper are referred to as the enhanced starting track event selection (ESTES) [10–18]. The selection criteria reject atmospheric muons and atmospheric neutrinos with accompanying muons in the southern equatorial sky, extending the measurement of the astrophysical diffuse flux down to 3 TeV.

Section II provides an overview of this paper's purposes and goals. Section III discusses the detector configuration and the simulated data used in this measurement. Section IV outlines how the neutrino energy and direction are reconstructed. Section V is a summary of the event selection. Section VI summarizes the likelihood techniques employed and how systematic uncertainties are incorporated. This is a binned-likelihood analysis based on expectations from simulated astrophysical neutrinos, atmospheric neutrinos and muons. Finally, Sec. VII discusses the results of the single power law, broken power law, hemisphere model, and unfolded flux measurements. A companion search for neutrino sources using the ESTES data selection is presented in an accompanying paper [19].

II. MEASUREMENT MOTIVATION

A. Astrophysical neutrinos

IceCube searches for neutrino sources have seen evidence for neutrino emission from TXS 0506 + 056 [20,21], NGC 1068 [22], and the Milky Way [23]. However, the flux measured from these three sources is only a small part of the total observed diffuse flux. Additional neutrino sources, potentially from multiple populations, are required to explain it in full [24–26].

IceCube finds the total astrophysical neutrino diffuse flux to be generally well described by a single power law, and no additional complexity has so far been established. However, there are reasons to believe that cosmic-ray accelerators could produce spectral features at TeV and sub-TeV energies, which motivates further detailed study of the diffuse flux [27].

In pp-scenarios, the cosmic rays interact with gas near the acceleration site. Neutrinos produced from pions and kaons follow the energies of cosmic rays, and the neutrino flux is expected with a similar spectral index as these cosmic rays [28]. A hardening of the flux is predicted below a break energy in specific models (motivated by cosmic ray diffusion), the neutrino flux is only expected to harden to a spectral index (γ) of ~ 2.0 below this break [29,30].

In pγ scenarios, the cosmic rays interact with a photon gas near the production site. This has been suggested to occur in cosmic ray reservoirs such as active galaxies (e.g. in NGC 1068) and other types of pγ sources [31–42]. The properties of the photon gas, in particular, the optical depth to photo-meson production, therefore drive the properties of the expected neutrino flux.

In either case, pp or pγ, the charged pions/kaons and muons can be further accelerated resulting in a hardening in the neutrino spectrum [43–47].

B. Starting track morphology

While astrophysical neutrinos are the target of this analysis, the largest contributors to the ESTES dataset below 100 TeV are atmospheric muons and atmospheric neutrinos. Atmospheric muons trigger the detector at a rate of 3000 Hz [48]. In comparison, approximately 100 astrophysical neutrinos are expected per year in this dataset. To improve signal purity, a series of complex cuts is deployed as described in detail in Sec. V.

Examples of strategies used recently by IceCube to measure the astrophysical diffuse flux are: a cascade dominated measurement [49], the selection of muon neutrinos from the northern sky [50], and the "starting event" selections [51,52,52,53]. The northern sky tracks dataset applies a cut in zenith to reject the overwhelming background from atmospheric muons. However, this data set is still dominated by atmospheric neutrinos at energies below 100 TeV.

One way to distinguish incoming neutrinos from downgoing muons uses an event signature where the interaction vertex can be located inside the detector. In contrast, incoming muons are removed if they have early photons recorded in the outer regions of the detector. The starting events selections [51–53] reduce the muon rate in the southern sky through veto techniques, whereby events are removed if they have early photons recorded in the outer regions of the detector. Retained events in [51–53] include both cascade and starting track events. These veto-based datasets also take advantage of the neutrino self-veto effect [54–56], which results in a suppression not only of atmospheric muons, but also of the atmospheric neutrinos in the southern sky due to the removal of atmospheric neutrinos that are accompanied by muons from the same shower. The self-veto was first implemented by the high energy starting events (HESE, [51]) analysis. A more complex veto was later constructed for the medium energy starting events (MESE, [52]) analysis, which applies a veto volume proportional to the charge of the event (lower charge, greater veto region size). While these datasets also allow for starting tracks, the rates are greatly reduced in the southern sky at lower energies due to their strict veto definitions.

The ESTES dataset takes advantage of the muon track topology to apply a dynamic veto and machine learning to greatly improve retention of starting track events in the southern sky. The dynamic veto is computed event-to-event
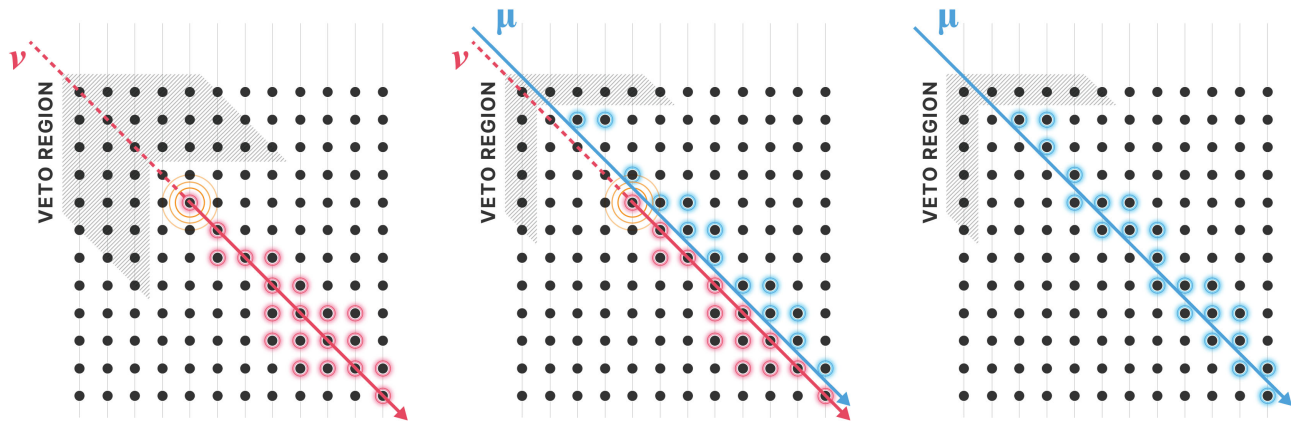
FIG. 1.   The diagram illustrates the concept of a dynamic veto region described in Sec. V B. The depth of the veto region depends on the location of the earliest hits and the total number of hits for a particular event. The orange circles indicate the presence of the hadronic shower from the muon neutrino interaction. Left: a muon neutrino interacts inside the detector. It leaves no light inside the veto region; therefore, the event is accepted. Center and right: an atmospheric muon will deposit light near the detector edge resulting in a much smaller veto region and high likelihood of light observed within the veto region (blue dots). This is true for events with a single muon (right), muon bundles, and atmospheric neutrinos with a coincident muon from the same air shower (center). These are rejected by the ESTES data selection.

using the position and direction of the first observed photon. The machine learning algorithms then use the distribution of the energy losses along the muon track and the positions to estimate the probability of a particular event being an astrophysical neutrino. This method allows measuring the astrophysical muon neutrino flux at lower energies. Figure 1 illustrates the differences between the ESTES target event morphology (left) and background morphologies (middle and right) present in the analysis.

Starting track events occur when a muon neutrino undergoes a charged current deep inelastic scattering interaction within the fiducial, or interior, volume of the detector. An initial cascade is observed from the hadronic component of the interaction followed by a muon track that eventually exits the detector. The presence of the cascade is advantageous as it gives us more access to the neutrino energy because a higher proportion of the neutrino's energy is deposited inside the detector. The exiting muon track is also useful since it is then used to reconstruct the neutrino direction.

An example of a starting track data event, which passed all cuts, is shown in Fig. 2. This event's reconstructed zenith angle is 71° and reconstructed neutrino energy, defined as the sum of the predicted cascade and muon energies, is 11 TeV respectively using the techniques discussed in Sec. IV.

III. DETECTOR AND SIMULATIONS

A. Detector configuration

The IceCube Neutrino Observatory is a cubic-kilometer sized detector located in the geographic South Pole buried 1.5 km under the Antarctic ice [57]. The detector is comprised of 5160 digital optical modules (DOMs), which each consist of a single photomultiplier tube (PMT) [58]

and associated data acquisition electronics [59]. As relativistic charged particles traverse the ice, the particles emit Cherenkov photons [60]. The DOMs will detect some of these photons, which are then converted by the readout system into an electronic signal. We refer to a discrete
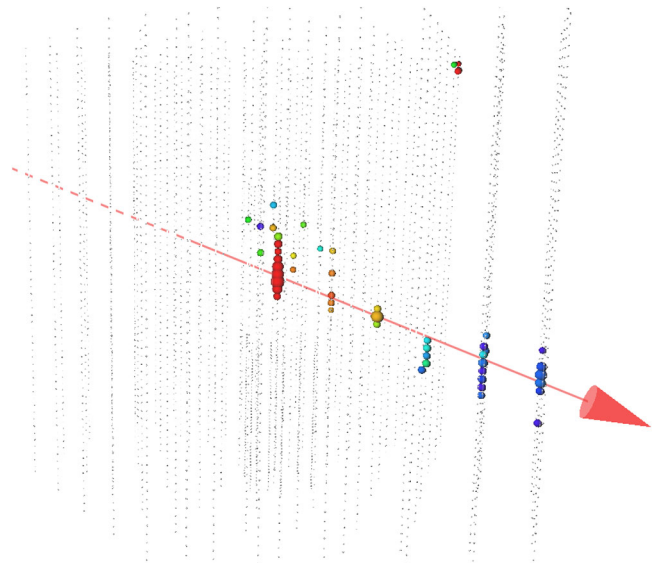
FIG. 2.   Event display of a data event satisfying the criteria for the ESTES data selection. Red represents the earliest light detected, while blue represents the last light detected. The reconstructed zenith angle is $\theta = 71°$, and the reconstructed neutrino energy (sum of the predicted cascade and muon energies) is $E = 11$ TeV. The dashed line is the reconstructed trajectory of the neutrino and the solid line is that of the reconstructed muon. The cluster of early hits (in red) is the cascade component, and the line of deposited charge is the track component. No charge is deposited in the outer layers (upper left) of the detector, which makes this a "starting" event.

signal in units of photoelectrons (PEs) and assign it a position and time.

The detector consists of a hexagonal grid of 86 instrumented cables referred to as strings [59]. The DOMs are spaced 17 m apart vertically on the strings, and the strings have a horizontal separation of 125 m. There is a central array, known as DeepCore, with 8 strings spaced about 70 m apart with each string containing 60 high quantum efficiency DOMs spaced about 7 m apart [61]. We use IceCube data collected from 2011-2022 and select runs where the entire 86-string detector was operational.

B. Simulation of neutrinos and atmospheric muons

To model the atmospheric neutrinos, produced through the interaction of cosmic rays with the atmosphere, we use the Gaisser H4a cosmic-ray model [62] and the Sibyll 2.3c hadronic interaction model [63] as a baseline. We use the matrix cascade equation solver (MCEq) software package [64] to compute the fluxes at the Earth's surface. MCEq allows us to compute the fluxes for various choices of cosmic ray and hadronic interaction models in a computationally reasonable way, since it does not simulate full cosmic ray air-showers. This is beneficial for parametrizing systematic uncertainties related to these models, as discussed in Sec. VI B. We define the conventional neutrino flux as the neutrinos from the decay of pions, kaons, and muons as the cosmic ray showers evolve in the atmosphere. The prompt neutrino flux is defined as the neutrino flux produced by the decay of charmed hadrons [4]. Interactions of neutrinos in the Earth are modeled assuming the Cooper-Sarkar-Mertsch-Sarkar (CSMS) neutrino-nucleon cross section [65] and preliminary reference Earth model (PREM) [66] Earth density model. Deep inelastic scattering interactions near (and inside) the detector are simulated using the NuGen software package [67]. For neutrinos with zenith angle < 90°, down-going neutrinos from the southern sky, we take into account the "self-veto" effect [54–56] using the Nu-Veto software package [56]. The self-veto effect is an analytical adjustment to the atmospheric neutrino flux after taking into account atmospheric muons from the same air shower and how efficiently we can tag and remove these types of events. We model the muon rejection probability using a Heaviside step function where all events containing a muon above a particular energy are rejected with a 100% probability. The self-veto effect is illustrated in Fig. 3 using $\eta_{\text{Self}-\text{Veto}} = 2.1$ (126 GeV), as defined in Sec. VI B.

The atmospheric muon events are simulated using MuonGun [68] for single muons and CORSIKA [69] for muon bundles. CORSIKA was used to validate the event selection performance in a background-dominated region and MuonGun was used to model the remaining muon background after all cuts were applied.

The charged leptons are propagated through the South Pole ice using PROPOSAL [70]. Cascade shower development is modeled using the Cascade Monte Carlo (CMC)
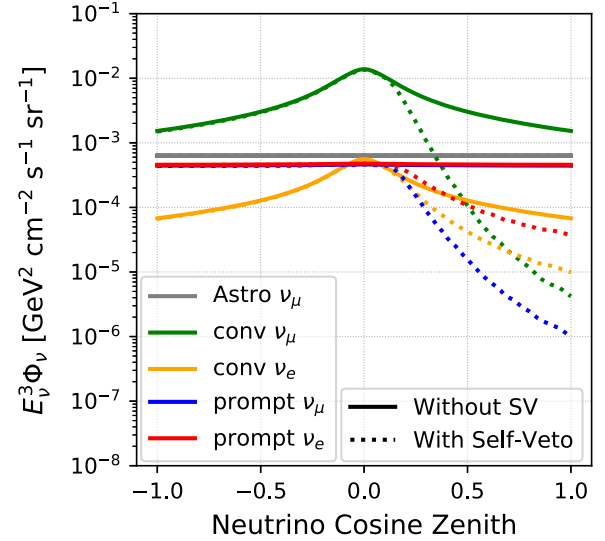

FIG. 3. Atmospheric neutrino fluxes with and without accounting for the self-veto. The astrophysical neutrino rate is higher than the atmospheric neutrino rate for events that pass the selection with energies of 50 TeV and above for cosine zeniths greater than 0.2 with the self-veto applied. (Note: matter effects not included here).

program [71]. The photons are propagated through the ice assuming a South Pole ice depth-dependent scattering and absorption coefficient [72,73].

IV. RECONSTRUCTED OBSERVABLES

The morphology of the observed light is used to reconstruct the event energy and direction of the charged particles. The observables described in this section rely on previously published IceCube algorithms. Some modifications to the algorithms have been made, to take advantage of the mixed properties of starting track events which can include light from a hadronic cascade and muon track. We discuss these modifications and the expected performance. We also rely on these reconstruction algorithms as seeds to more complex observables used in the event selection. In Sec. V, these will be explicitly defined.

A. Directional reconstruction

The direction of the event is reconstructed using a series of increasingly complex algorithms. Initial directional reconstructions are performed using the LineFit [74,75], SPEFit [76], SplineMPE [76], and Millipede [77] algorithms with each subsequent algorithm seeded by the track direction found using the previous algorithm. The most complex directional algorithm Millipede takes into account all active DOMs in the detector, regardless of whether they observe a signal or not, to compute the overall direction and energy of the track. Millipede works by splitting up the track into segments and fitting an independent energy loss for each segment, thus accommodating the stochastic

nature of the energy loss of muons. Millipede is run once to calculate the track direction and a set of energy losses along the track. This is then used to compute many of the starting tracks BDT inputs as described in Sec. V C.

However, the hadronic cascade at the neutrino interaction vertex can introduce an incorrect initial track direction for events with shorter track lengths. Also, neutrino events with coincidental muons (not from the same air shower) often result in incorrect directions due to the presence of the photons from the second track. We, therefore, introduce a refined reconstruction that is a sequence of three algorithms: (1) iterative-SplineMPE [76], (2) f_{hit} algorithm to select the "best track" from a list of tracks, (3) Millipede using the "best track" as a seed.

The iterative-SplineMPE algorithm is adopted from Ref. [76]. This algorithm attempts to find a global zenith angle by refitting the track using different zenith angles, azimuth angles, and positions randomly selected and connecting it to the previous best-fit vertex. For each tested track, if the likelihood shows improvement, then this new track is chosen as the best track. If no improvement is seen over 50 iterations, then this iterative-SplineMPE is passed to the next step.

The quantity f_{hit} is then computed for a predefined list of tracks (LineFit, SPEFit, SplineMPE, iterative-SplineMPE, and Millipede). To calculate f_{hit}, we take a reconstructed track hypothesis and find all DOMs within a perpendicular distance r along the reconstructed track. This is a cylinder centered around the track with radius r. The f_{hit} is defined as the fraction of DOMs that detect at least one hit within this radius r cylinder. The f_{hit} distribution is defined for different choices of r (100 m, 200 m, etc.). The track with the greatest cumulative f_{hit} is selected as the "best track". This best track is then used as the seed to the Millipede algorithm again. The resulting direction from this Millipede fit is then used as the observable for the flux measurement. The angular resolution achieved using this procedure is shown in Fig. 4. The directional resolution for this procedure is 1.5° at 1 TeV and 0.66° at 100 TeV for starting track events.

B. Energy reconstruction

The distribution of energy losses for the event is first calculated using the Millipede algorithm [77] from Sec. IV A. Millipede was set to compute the deposited energy every 10 m along the track direction. The energy loss per segment is then used to train a random forest [78,79] to predict the energy from the hadronic and muonic components separately [53]. Here, the muon energy is defined as the muon's energy at its creation. We take the sum of the predicted cascade and muon energies to define the "reconstructed energy" of each event. Figure 5 shows the reconstructed energy as a function of the true neutrino energy assuming muon neutrino events only.

The energy resolution for this dataset is 25% at 1 TeV and remains almost constant up to ~1 PeV. The top panel
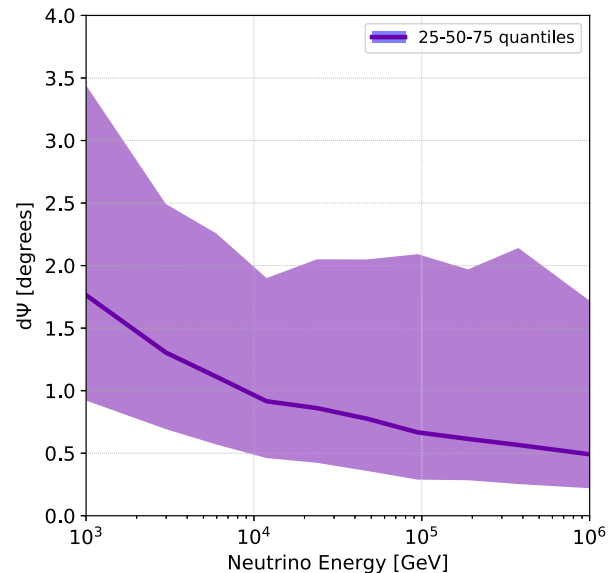

FIG. 4. Directional error 25, 50, 75% quantiles for starting muon neutrinos as a function of the real neutrino energy. $d\psi$ is the space angle distance between the reconstructed direction and the truth direction. At 1 TeV the events are reconstructed with a median resolution of 1.6°, at 100 TeV we see a median resolution of 0.66°.

of Fig. 5 shows a slight biasing toward reconstructing higher energies at 1 TeV. Above 1 PeV, the energy resolution degrades to 30%. This loss in resolution is due to the increasing amount of energy the muon escapes the detector with. However, the achieved energy resolution of ~25–30% is a significant improvement over that which is traditionally achieved using track events [50,80,81].

V. EVENT SELECTION

A. Quality cuts

Observed photons are recorded in units of PEs after taking into account quantum efficiency and calibration effects [82]. The IceCube detector trigger requires at least 8 locally coincident DOM hits recorded within a 5 microsecond window. After the trigger, an event is processed through the IceCube filtering scheme. There are many different filters which all involve fast selection criteria relying on basic event properties. Each filter targets different event morphologies. The ESTES dataset selects events which pass at least one of the following filters: muon-filter or full-sky-starting-filter [83]. One further quality cut is applied to the data set before the specific starting track event veto criteria are implemented. This cut is based on a quantity called the "homogenized total charge" (HQTot). HQTot is calculated by summing all detected PEs, without DeepCore and excluding DOMs where the sum of PEs in a single DOM is more than 50% of the total charge of the event because of their negative impact on reconstruction quality. We select events where HQTot is more than
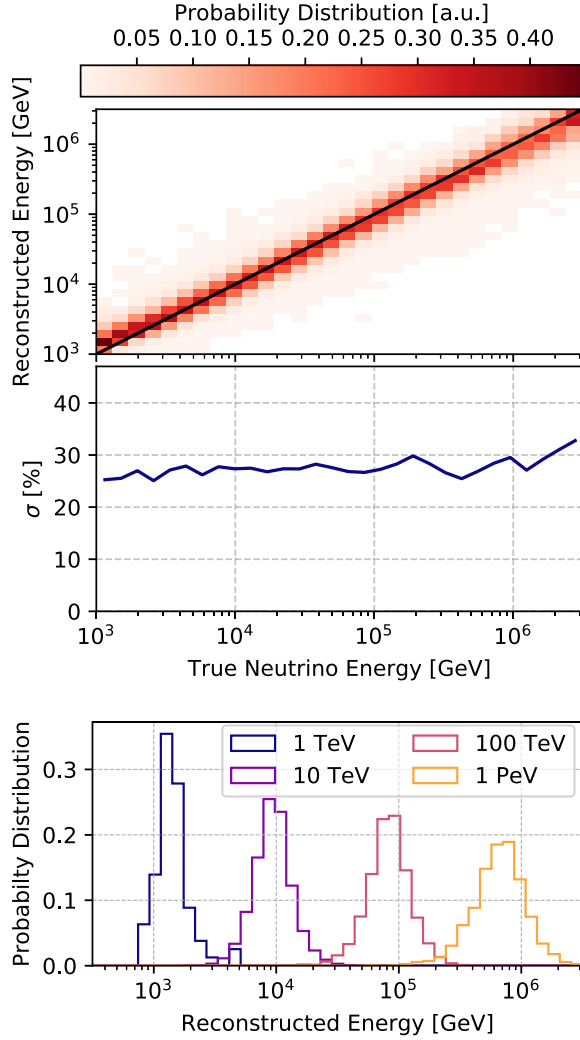
FIG. 5. Top: reconstructed event energy shown as a function of true neutrino energy. For each true neutrino energy slice, the distribution of events is normalized. The energy resolution (σ) for starting track events is observed to be near 25% for 1 TeV and worsens to 30% above 1 PeV. This is due to the increased amount of energy the muon eventually exits the detector with for higher energy events. Bottom: slices of reconstructed event energies for neutrinos with true energy 1 TeV, 10 TeV, 100 TeV, and 1 PeV. We observe a slight loss in energy resolution toward higher energies.

200 PE, which removes low charge events susceptible to large systematic uncertainties and poorly reconstructed observables. These quality cuts cumulatively reduce the atmospheric muon rate from 3 kHz to 0.1 Hz.

B. Starting track veto

We now define the starting track veto (STV) as diagrammed in Fig. 1 (first proposed in reference [10]). A veto region is constructed for each event taking into account the location of the first in-time observed photon and the expected light emission profile of an incoming muon track.

This dynamic veto allows us to retain a good efficiency for astrophysical neutrinos toward lower energies while still significantly reducing the atmospheric muon and neutrino rate.

The SplineMPE reconstructed muon track [76] is used to identify the position, direction, and time of the expected muon track. Each DOM is then assigned a probability distribution of PEs that would be expected from this muon track. This is shown as the red curves (expected PE) in the lower panels of Fig. 6 and the 90% PE expectation is shown as a gray time window. We find the first PE in the event that can be produced by this muon track (earliest in-time hit) within the allowable time windows. Using the track direction, earliest in-time hit position, and Cherenkov cone geometry, we define the "veto-region" as the region where light should be observed assuming this particular light profile is from an incoming muon track. In the case of an actual incoming muon track, the probability of observing light in this veto-region is high. If the first hit is observed in an outer layer DOM, the event is also likely to be marked as an incoming muon. Meanwhile, the probability of observing light in this veto-region is low for a starting track event. Figure 6 shows three reference DOMs for a starting track event: one before the neutrino interaction takes place, one at the location of the first observed PE, and one with multiple PEs observed. There are PEs observed in the veto region at later times from scattered photons from the hadronic shower development (or from noise), but these hits would not be included in the time window since they occur much later than hits predicted from a muon track.

The probability that a DOM detects a photon is modeled using a Poisson probability where the expected number of PEs (λ) follow the assumption that a through-going muon track actually emitted Cherenkov light. The expected number of these photons at each DOM is calculated using position, direction, timing, and energy of the particle that emitted them (e.g. higher energy particles emit more photons, particles near a DOM have a greater chance of detection). The likelihood is now defined as the product of all Poisson probabilities for all DOMs in the veto-region (VR-DOMs). This likelihood, p_{miss}, is defined as:

$$p_{\mathrm{miss}}(k = 0, \lambda_i) = \Pi_i^{\mathrm{VR\text{-}DOMs}} \frac{e^{-\lambda_i} \lambda_i^k}{k!} \qquad (1)$$

with the performance shown in Fig. 7. p_{miss} is a measurement of the probability that VR-DOMs saw no light assuming the event was throughgoing; therefore we set $k = 0$ for all VR-DOMs. p_{miss} values closer to 0 are defined as more "startinglike" while values closer to 1 are defined as more "throughgoinglike," events that have their interaction vertex outside of the detector's volume. We note that the presence of noise hits is negligible as the noise hit would need to occur in-time with the track to affect the placement of the vertex. Noise hits can enter the veto region
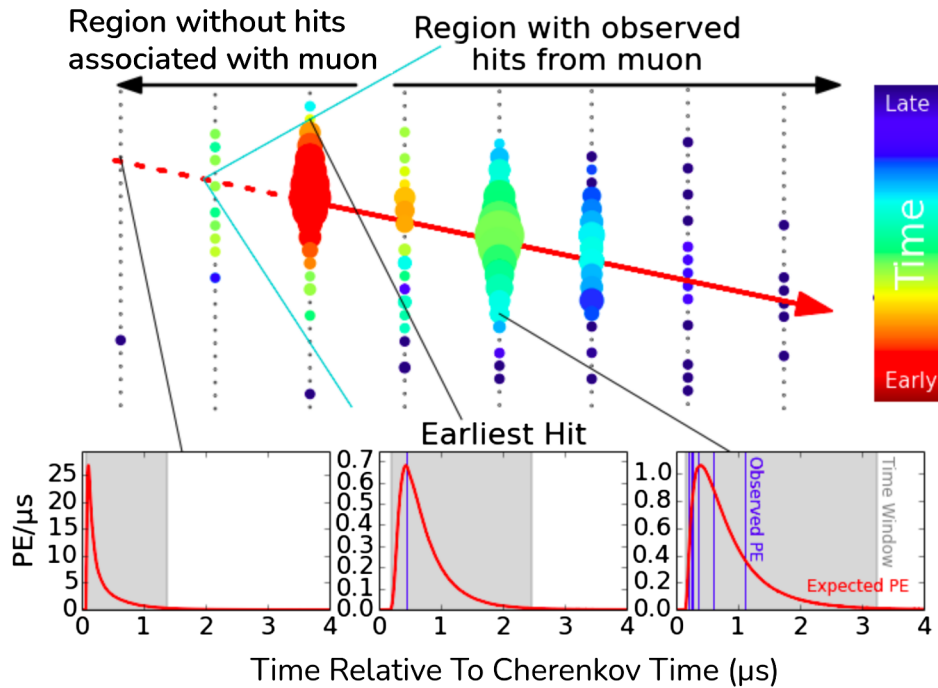
FIG. 6. Diagram of a starting track event, the dashed red line shows the incoming neutrino and the solid red line shows the outgoing muon track. In the lower panel, the PE probability distributions for 3 reference DOMs are shown in red (assuming the muon track emits all light) and the observed hits are show as purple vertical lines. The earliest possible hit from a muon track is then connected to the track along the Cherenkov cone direction and used to define the "veto-region". The inferred direct Cherenkov emission cone is delineated by the cyan lines. The gray shaded regions in the sub-figures denote the time-windows corresponding to 90% of the expected PEs. We see there are hits in the veto region that occur at much later times. These PEs, likely to be from the hadronic shower development, are excluded due to this time-window criteria.
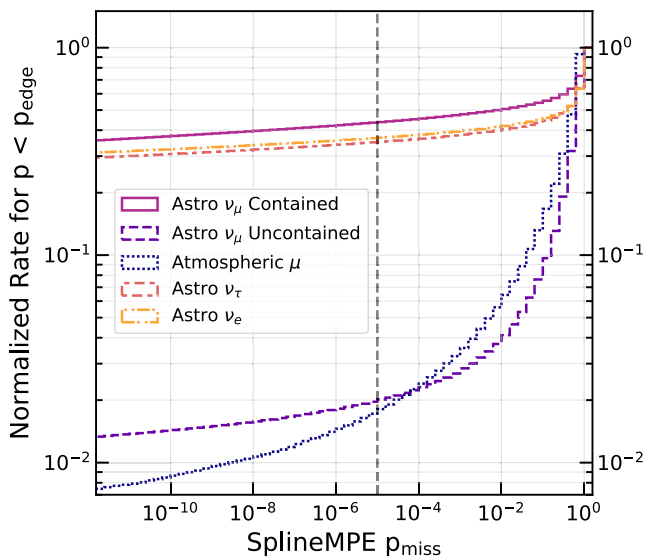

FIG. 7. p_{miss} distribution for atmospheric muons and astrophysical neutrinos. A cut requiring events to have $p_{miss} < 10^{-5}$ reduces atmospheric muon rates by three orders of magnitude while retaining a high signal efficiency for muon neutrino events with interaction vertices contained inside the detector volume. This figure is normalized to show p_{miss} shape differences between the interaction types.

by chance but the number of DOMs in the veto region is large enough such that this is a negligible effect. A cut of $p_{miss} = 10^{-5}$ was found to be optimal to reduce the incoming muon rates by 2 orders of magnitude while removing very little starting astrophysical neutrino events. In addition to defining a p_{miss}, we can also use the reconstructed vertex and direction of the muon track to estimate the length of the muon track inside the detector. A cut of 300 m is applied to ensure the track is of sufficient length to predict its energy and direction.

Poorly reconstructed muons can pass this veto criteria if the track enters through a corridor in the detector. These corridors are defined as regions of uninstrumented detector, passing directly between adjacent rows or vertical columns of instrumented strings due to the detector's hexagonal grid. To combat this, we connect the center of gravity of charges of the event to a predefined list of these corridors. These new tracks are then refit using the same SplineMPE algorithm as before. For all events, we make a list of tracks with a reconstruction likelihood value within 2% of the maximum likelihood, p_{miss} and the track length are calculated for this list. Events with a track length below 300 and events with a p_{miss} above 10^{-5} are rejected. The maximum p_{miss} from this procedure is then used as an input to the BDT as described in Sec. V C.
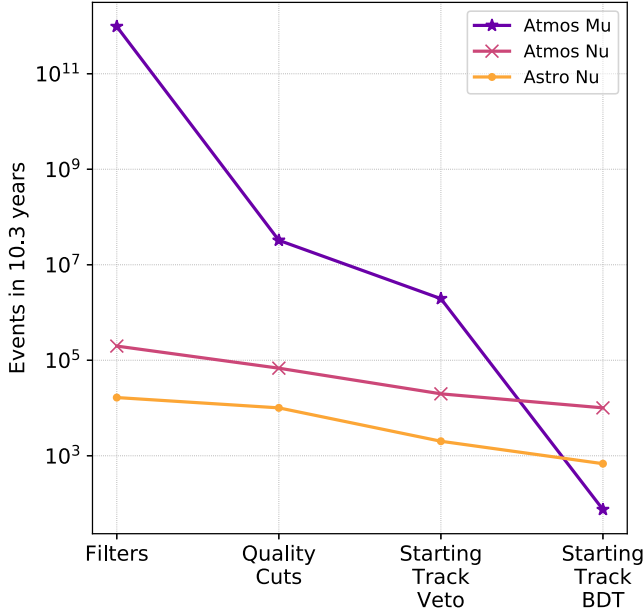
FIG. 8.   Summary of all cuts as described in Sec. V. We start with an overwhelming atmospheric muon rate where the muons outnumber the neutrinos by at least 5 orders of magnitude. After applying all the cuts, the neutrinos outnumber the muons by 2 orders of magnitude. The MC expectation shown is pre-fit and shown for illustrative purposes only.

Finally, the starting track veto is used with a more detailed muon light emission profile. Most importantly, this improves the reconstruction of the vertex position. We then take the same set of tracks that were selected from the corridor scan and now compute the p_{miss} for each track, only keeping the maximum p_{miss} from this list of tracks and this muon light emission profile. The maximum p_{miss} is not used as a cut, however this is saved for use in the BDT as described in Sec. V C.

C. Starting tracks boosted decision tree

After the initial quality and veto cuts, the atmospheric muon rates are still ~4 orders of magnitude higher than the expected astrophysical neutrino rate. We have removed atmospheric muons that deposit light close to the detector edge but there is still a significant number of difficult-to-detect muons remaining. To reduce this background, we use the XGBoost boosted decision tree (BDT) algorithm [84] to classify events as atmospheric muons or starting muon-neutrino charged current events. We use a simulated dataset with 1 million atmospheric muons and 200,000 starting muon-neutrino charged current events to train the BDT. The dataset was split into 70/30 training/validation where the training set was used to train the BDT and the validation set was only used to select the optimal model after hyper-parameter and input variable optimization. An independent MC set with over 900,000 events was later used for the measurement. The thirteen variables used are shown in Appendix A.

TABLE I.   The observed data events and fitted MC events broken up by type. The left column has an additional cut on zenith $<80°$ to emphasize the higher proportion of astrophysical neutrinos in the southern sky.

	Events $\theta < 80°$	All events
Astro Nu	298	680
Atmos Conv. Nu	980	10042
Atmos Conv. Mu	42	75
Total MC	1320	10797
Data	1365	10798

Atmospheric muons with zenith $(\theta) > 80°$ are almost all poorly reconstructed events and the characteristics of such events are greatly different from atmospheric muons with $\theta < 80°$ which tend to be difficult-to-detect muons. The number of atmospheric muons expected greatly differs by angle; we therefore use the precision-recall area under the curve evaluation metric [85] to optimize the BDT. After training, a single BDT model is used but with different cuts on BDT score for each hemisphere ($\theta > 80°$ and $\theta < 80°$). Using the best-fit single power law flux parameters as described in Table III, we show the sorted BDT features in Table VI. The performance of the BDT using 1 year of IceCube data was shown in Refs. [15,18].

Figure 8 summarizes the event rates from cut to cut. We see significant decrease in muon rates at each cut at the cost of some neutrino events. After applying all cuts, the muons make up $<1\%$ of the final event rate. 10798 data events are observed between 1 TeV and 10 PeV over the entire sky. Table I summarizes the observed data rates compared to the rates as computed from the MC using the best-fit parameters from Table III.

VI. MEASUREMENT METHODOLOGY

A. Statistical analysis

The measurement of the diffuse flux utilizes the forward folding likelihood technique. All simulated and observed data events are placed into two-dimensional binning as summarized in Table II, totaling 190 bins. Each bin has a corresponding expectation value as computed using simulated data. The simulated data is a sum of the astrophysical neutrinos, atmospheric conventional

TABLE II.   Summary of 190 bins used to define observed and expected number of events in the likelihood Eq. (3). One overflow bin is used to capture events from 1 PeV to 10 PeV.

Observable	Bin range	Number of bins
Energy	1 TeV to 1 PeV	18 (log) [+1 overflow]
Cosine Zenith	−1 to 1	10 (linear)

neutrinos, atmospheric prompt neutrinos, and atmospheric muons:

$$\lambda = \lambda_{\text{Astro}} + \lambda_{\text{Conv}} + \lambda_{\text{Prompt}} + \lambda_{\text{Muon}}. \qquad (2)$$

Each of these terms is modified according to a flux normalization (atmospheric component and astrophysical component) and spectral index (astrophysical component only).

We now define the probability of having observed k events while expecting λ-events using a Poisson probability. The likelihood function is defined as the product of all 190 Poisson probabilities. To take into account systematic uncertainties (nuisance parameters), described in greater detail in Sec. VI B, we introduce a modification to our expectation value $\lambda = \lambda(\eta, \epsilon)$. The set of η, ϵ are summarized in Table III. The ϵ parameters are aided by external measurements using a Gaussian function ($\mathcal{N}$) with a mean (μ) and standard deviation (σ) to constrain the likelihood. Nuisance parameters without external constraints are modeled using a uniform distribution (η). The modified likelihood function including these modifications is:

$$\mathcal{L}(\lambda(\eta, \epsilon)|k) = \Pi_{i=1}^{190}\left(\frac{e^{-\lambda_i}\lambda^k}{k!}\right) \cdot \Pi_{j=1}^{6}\frac{e^{-(\epsilon_j - \mu_j)^2/2\sigma_j^2}}{\sigma_j\sqrt{2\pi}}. \qquad (3)$$

To compute the parameters $\hat{\Theta}$ that best describe the data, we run a minimization of the negative log of the likelihood function using the Minuit2 C++ library [86,87]. To compute the confidence intervals on the best fit set of parameters, we use the profile likelihood technique. The likelihood is now defined as the likelihood with the set of parameters Θ such that the likelihood function is once again maximized. We define the test-statistic for this measurement as the negative log likelihood ratio of this likelihood function at Θ with respect to the likelihood function at $\hat{\Theta}$. This test-statistic is:.

$$\mathcal{TS}(\Theta) = -2\log\left(\frac{\mathcal{L}(\lambda(\Theta)|k)}{\mathcal{L}(\lambda(\hat{\Theta})|k)}\right). \qquad (4)$$

The confidence intervals are then presented using Wilks' theorem [88].

B. Systematic uncertainties

The ESTES data selection is a significant increase in the total number of events as compared to previous starting-event event selections. This large increase motivated an expanded treatment of systematic uncertainties. A summary of all parameters (pre)postfit is available in Table III. The last column shows the best-fit points after the measurement is performed with 68% confidence

intervals as defined in Sec. VI A. When relevant, the $\pm 1\sigma$ constraints are shown as 2D templates in Appendix C.

Further details about the atmospheric flux systematics can be found in Appendix B and are briefly summarized as:

(i) Φ_{conv}, Φ_{prompt}, and Φ_{muon} are normalization factors for their respective flux components, using the Gaisser H4a cosmic ray [62] and Sibyll 2.3c hadronic interaction [63] models.

(ii) $\epsilon_{\nu\bar{\nu}\text{-ratio}}$ controls the relative contributions from atmospheric neutrinos to anti-neutrinos, $\epsilon_{\nu\bar{\nu}\text{-ratio}} = 2\nu/(\nu + \bar{\nu})$.

(iii) ηH4a-GST interpolates between the flux predictions of the H4a and GST cosmic ray flux models.

(iv) η2.3c-DPMJet interpolates between the flux predictions of the Sibyll 2.3C and DPMJet hadronic interaction models.

(v) $\eta_{\text{Self-Veto}}$ weakens and strengthens the muon rejection probability function used in the self-veto effect. The value corresponds to the muon energy used in a Heaviside function.

Further details about the detector systematics can be found in Appendix C, and are briefly summarized as:

(i) $\epsilon_{\text{Scattering}}$ and $\epsilon_{\text{Absorption}}$ scale the scattering and absorption of photons in the bulk ice (ice between detector strings) according to a depth dependent parameterization that accounts for the effect of glacial ice impurities and structural properties on photon propagation.

(ii) $\epsilon_{\text{Angular,DOM}(p_0)}$ and $\epsilon_{\text{Angular,DOM}(p_1)}$ model the angular response function of the IceCube DOMs, due to the photomultiplier tubes pointing downward (causing zenith angle dependence) and the impurities of the columns of refrozen ice containing the DOMs.

(iii) $\epsilon_{\text{Overall,DOM}}$ is an overall scaling factor applied to all IceCube DOMs, representing the cumulative systematic error of the absolute sensitivity of the sensor, including the uncertainties on the photomultiplier tube's quantum efficiency.

VII. DIFFUSE FLUX MEASUREMENT

A. Measurement of the diffuse flux assuming a single power law flux

A search for the astrophysical neutrino flux is first performed under an isotropic single power law flux (SPL) hypothesis, and the best-fit SPL parameters are determined to be

$$\Phi_{\text{Astro}}^{\text{Total}} = \phi_{\text{Astro}}^{\text{per-flavor}} \times \left(\frac{E_\nu}{100 \text{ TeV}}\right)^{-\gamma} \times C_0,$$

$$C_0 = 3 \times 10^{-18} \times \text{GeV}^{-1} \text{ cm}^{-2} \text{ s}^{-1} \text{ sr}^{-1}$$

where,

$$\phi_{\text{Astro}}^{\text{per-flavor}} = 1.68^{+0.19}_{-0.22}, \qquad \gamma = 2.58^{+0.10}_{-0.09} \qquad (5)$$

TABLE III.　Summary of all parameters used in the measurement of the astrophysical diffuse flux using a single power law. All parameters with constraints are modeled as a Gaussian penalty term in the likelihood. All parameters are assumed to be independent.

Parameter	Boundary	Constraint ($\mu \pm \sigma$)	Best-fit	Description
Astrophysical Flux Parameters				
Φ_{Astro}	$[0, \infty)$	$\cdots$	$1.68^{+0.19}_{-0.22}$	Astrophysical neutrino flux normalization
γ_{Astro}	$[0, \infty)$	$\cdots$	$2.58^{+0.10}_{-0.09}$	Astrophysical neutrino flux spectral index
Atmospheric Flux Parameters				
Φ_{muon}	$[0, \infty)$	$\cdots$	0.6 ± 0.4	Atmospheric muon flux normalization
Φ_{conv}	$[0, \infty)$	$\cdots$	1.5 ± 0.3	Atmospheric conventional neutrino flux normalization
Φ_{prompt}	$[0, \infty)$	$\cdots$	<3.19 (90% U.L.)	Atmospheric prompt neutrino flux normalization
$\epsilon_{\nu\bar{\nu}\text{-ratio}}$	$[0,2]$	1 ± 0.10	1.04 ± 0.08	$\nu\bar{\nu}$-ratio
$\eta_{\text{H4a-GST}}$	$[-2, +1]$	$\cdots$	-1.4 ± 0.4	H4a-GST cosmic ray flux model interpolation
$\eta_{\text{2.3c-DPMJet}}$	$[-2, +1]$	$\cdots$	-0.6 ± 0.6	2.3c-DPMJet hadronic interaction model interpolation
$\eta_{\text{Self-Veto}}$	$[1, 3]$	$\cdots$	$2.1^{+0.1}_{-0.3}$	Self-veto muon rejection intensity, $\log_{10}\left(\frac{\text{Energy}}{1\,\text{GeV}}\right)$ units
Detector Systematic Parameters				
$\epsilon_{\text{Scattering}}$	$[0.8,1.2]$	1 ± 0.05	1.04 ± 0.03	Bulk-ice model scattering coefficient scaling
$\epsilon_{\text{Absorption}}$	$[0.8,1.2]$	1 ± 0.05	0.98 ± 0.03	Bulk-ice model absorption coefficient scaling
$\epsilon_{\text{Angular,DOM(p}_0)}$	$[-0.5, 0.3]$	-0.3 ± 0.5	-0.3 ± 0.3	Angular PM acceptance parameter p0
$\epsilon_{\text{Angular,DOM(p}_1)}$	$[-0.10, 0.05]$	-0.04 ± 0.10	-0.09 ± 0.05	Angular PM acceptance parameter p1
$\epsilon_{\text{Overall,DOM}}$	$[0.8,1.2]$	1 ± 0.10	0.91 ± 0.05	Absolute DOM acceptance

This model (and all following models) assume $\nu_e : \nu_\mu : \nu_\tau = 1:1:1$ and $\nu:\bar{\nu} = 1:1$ arriving at the surface of the Earth. In Eq. (5), $\phi_{\text{Astro}}^{\text{per-flavor}}$ refers to the per-flavor normalization ($\nu + \bar{\nu}$) and is defined as a unit-less number. We introduce C_0 as a constant that carries the units for the diffuse flux and a factor of 3 to compensate for the three flavors. Unless explicitly defined otherwise, whenever we refer to the astrophysical normalization we are referring to the per-flavor normalization.

All of the parameters and their 1σ confidence intervals are shown in Table III. The two-dimensional confidence intervals for the two parameters of interest are shown in Fig. 9 using the profile likelihood assuming Wilks' theorem. A comparison of the 68% confidence intervals to the most recent IceCube results is shown in Fig. 13 and discussed in Sec. VII F. Using the best-fit parameters, we now compare the simulated data to the observed data in Fig. 10 for energy and cosine zenith distributions of the events. A goodness of fit test with a p-value = 0.7 using the saturated Poisson likelihood test [89] confirms excellent agreement between the data and simulation. Further validation of the measurement is detailed in Appendix D.

The 90% sensitive energy range for the astrophysical flux model is 3–550 TeV using the techniques described in [90], reaching lower energies than previous diffuse analyses in IceCube [49–51]. We show this energy range as a blue shaded region and solid lines in Fig. 11. We remind the reader that the previous lowest energy flux measurement was dominated by cascades (electron and tau neutrinos), a dedicated discussion of these differences is in Sec. VII F. Despite these differences in sensitive energy

ranges, the previous IceCube single power law flux measurements are consistent with this measurement.

B. Measurement of the diffuse flux assuming a segmented power law

We now characterize the astrophysical flux with an isotropic, segmented power law over 1 TeV–100 PeV, defined as a step-function of single power law fluxes fixed
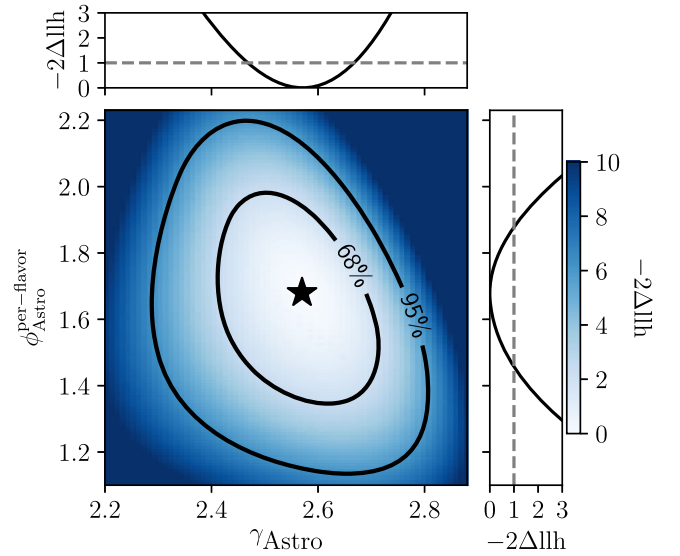

FIG. 9.　Single power law flux likelihood scan shown in 1D and 2D. Wilks' theorem is used to define the 68% and 95% confidence intervals. The best-fit normalization and spectral index is shown as a black star.
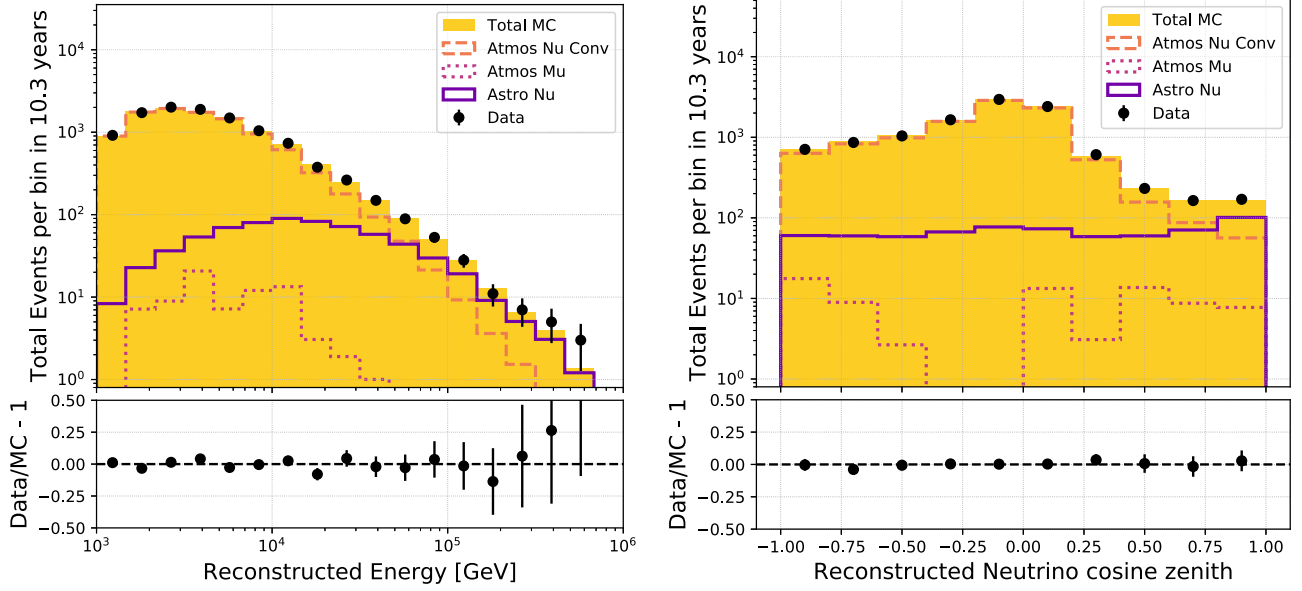
FIG. 10. The reconstructed energy and cosine zenith distributions for data and simulated data using the best-fit parameters from the single power law flux measurement. The astrophysical neutrinos are shown as a solid purple line, the atmospheric neutrino and muon expectations are shown as dashed and dotted lines respectively. The error bars shown for data are due to Poisson statistics only.

at $\gamma = 2$, with two measured bins per energy-decade, as shown in Eq. (6):

$$\Phi_{\text{Astro}}^{\text{Total}} = \Sigma_{i=1}^{8} \phi_i \times \left(\frac{\text{E}_{\nu,i}}{100 \text{ TeV}} \right)^{-2} \times C_0. \qquad (6)$$
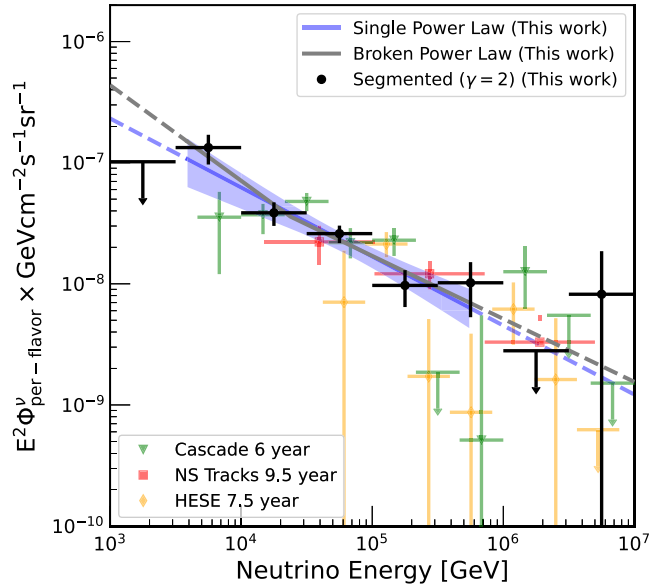

FIG. 11. The per flavor astrophysical neutrino flux shown as a function of energy. The black points are the segmented power law flux measurement assuming a spectral index of −2. The blue line with error bands corresponds to the SPL measurement as shown in Fig. 9. The blue shaded region is the 90% sensitive energy range. The gray line is a fit to data assuming a broken power law flux. We include results from recent IceCube publications for direct comparison [49–51].

The measured results, $\text{E}_{\nu,i}$ and ϕ_i (ν:$\bar{\nu}$), are defined in Table IV. The width of each bin was chosen such that we minimized bin-to-bin correlations. This measurement was performed over the entire sky with all nuisance parameters from Table III, and it allows us to quantify energy dependent effects on the flux in a model-independent way.

For each ϕ_i, a range of neutrino energies is used. When plotting each normalization in Fig. 11, the median energy for these energy ranges in log-space is used to compute the total astrophysical flux per flavor. When the best-fit $\phi_i = 0$, a 68% upper limit is quoted. All segments are consistent with the single power law flux measurement, indicating a lack of evidence for energy dependent structure beyond a

TABLE IV. The results of the segmented power law fit as show in Fig. 11. All normalization components are fit simultaneously including all systematic uncertainties from Table III. The uncertainties are the 68% confidence intervals assuming Wilks' theorem. The rightmost column compares the segmented power law fit with a refit done using a galactic plane Gaussian prior term described in Sec. VII D.

Bin_i	$Energy_{\nu,i}$	Energy range	ϕ_i ($\pm 1\sigma$)	$\frac{\phi_{i,GP} - \phi_i}{\phi_i}$
1	1.78 TeV	[1–3.16 TeV]	$0.0^{+10.2}_{-0}$	0%
2	5.62 TeV	[3.16–10 TeV]	$13.3^{3.67}_{-3.67}$	−3.99%
3	17.8 TeV	[10–31.6 TeV]	$3.86^{+0.85}_{-0.85}$	−14.44%
4	56.2 TeV	[31.6–100 TeV]	$2.60^{+0.43}_{-0.43}$	−7.57%
5	178 TeV	[100–316 TeV]	$0.97^{+0.33}_{0.33}$	−7.22%
6	562 TeV	[316 TeV–1 PeV]	$1.02^{0.49}_{-0.49}$	−1.96%
7	1.78 PeV	[1–3.16 PeV]	$0.00^{+0.28}_{-0}$	0%
8	5.62 PeV	[3.16–10 PeV]	$0.82^{+1.04}_{-0.82}$	−26.83%

single power law. Previous IceCube measurements are shown for direct comparison [49–51], and they also did not find any evidence beyond the single power law. We note each dataset used different bins for their analysis given their various strengths and weakness, further discussed in Sec. VII F. An analysis of IceCube cascade events [49] found hints of a hardening of the flux toward lower energies but we do not observe this hardening in this sample. The compatibility of the data samples is discussed in greater detail in Sec. VII F.

At the highest energies, a nonzero flux was observed from 3–10 PeV. This measurement is consistent with the Glashow resonance (GR) [91] flux measurement from IceCube [92]. Monte Carlo only studies found the most likely GR event topology is from $\bar{\nu}_e + e \rightarrow W \rightarrow \mu + \nu_\mu$ or $\bar{\nu}_e + e \rightarrow W \rightarrow \tau + \nu_\tau$ where the τ decays leptonically $\tau \rightarrow \nu_\tau + \mu + \nu_\mu$. This starting track would have no hadronic shower but would still contain an energetic muon track [93]. The resulting muon would only carry about 100–500 TeV of the initial neutrino energy preventing us from identifying the single data event using the data sample as presented in this work.

C. Measurement of the diffuse flux assuming a broken power law

We now characterize the astrophysical flux with an isotropic, broken power law (BPL),

$$\Phi_{\text{Astro}}^{\text{Total}} = \phi_0 \times \left(\frac{E_{\text{break}}}{100 \text{ TeV}}\right)^{-\gamma_2} \times C_0,$$

$$\phi_0 = \begin{cases} \phi_{\text{per-flavor}}^{\text{Astro}} \times \left(\frac{E}{E_{\text{break}}}\right)^{-\gamma_1} (E < E_{\text{break}}), \\ \phi_{\text{per-flavor}}^{\text{Astro}} \times \left(\frac{E}{E_{\text{break}}}\right)^{-\gamma_2} (E > E_{\text{break}}). \end{cases} \quad (7)$$

This model assumes there are two spectral indexes, one for neutrino energies below an energy break and a second spectral index that extends to higher energies with the normalization defined at the energy break. The parameters to be fit are the flux normalization $\phi_{\text{per-flavor}}^{\text{Astro}}$ ($\nu{:}\bar{\nu}$), the energy break E_{break}, and two spectral indices γ_1 and γ_2 with the following best fits:

$$\phi_{\text{per-flavor}}^{\text{Astro}} = 1.7^{+0.19}_{-0.22}, \qquad \log_{10}\left(\frac{E_{\text{break}}}{1 \text{ GeV}}\right) \sim 4.36,$$

$$\gamma_1 = 2.79^{+0.30}_{-0.50}, \qquad \gamma_2 = 2.52^{+0.10}_{-0.09}. \quad (8)$$

The BPL model allows a model independent probe of structure in the flux. Structure is expected in some models toward lower energies. For example in some scenarios, the neutrino flux is expected to continue toward lower energies [28,94] until it reaches an energy break and falls off rapidly to $\gamma \sim 0$ [95] below this break.

When fitting a broken power law, we observed a slight softening of the spectrum below the energy break, $E_{\text{break}} = 23$ TeV. The test-statistic that the BPL is preferred over the SPL is 0.4, which is not statistically significant. As a result, E_{break} is poorly constrained, so we quote only the best fit point. The errors on γ_1 and γ_2 are at that fixed E_{break} from one-dimensional profile likelihood scans. We use this data to reject $\gamma_1 < 0$ to 3.4σ significance and $\gamma_1 < 1$ to 3.0σ at an energy break of 23 TeV. $\gamma_1 < 2$ is only rejected to a 2.1σ level. A summary of the various energy breaks tested with the corresponding best-fit spectral indexes is shown in Fig. 12. These results do not indicate any sign of the neutrino flux falling off below 23 TeV.

An analysis where the BPL model is relevant is that performed by Fang *et al.* [96]. We know the production mechanisms by which neutrinos are produced are from either pp or pγ processes. In pγ scenarios, protons interact with the photons near the source through photo-pion production only when their energy is above the pion production threshold [96]. In these scenarios, Fang *et al.* use IceCube and Fermi data to predict that the gamma ray flux generated in the source region must cascade down to MeV-GeV energies as to not violate the observed extra-galatic Fermi gamma-ray data [27,97,98]. The ESTES BPL observations (a lack of hardening in the fitted spectrum below the energy break), under these gamma ray flux interpretations, imply that the dominant neutrino sources are opaque to gamma rays [27,28,99]. One example is NGC
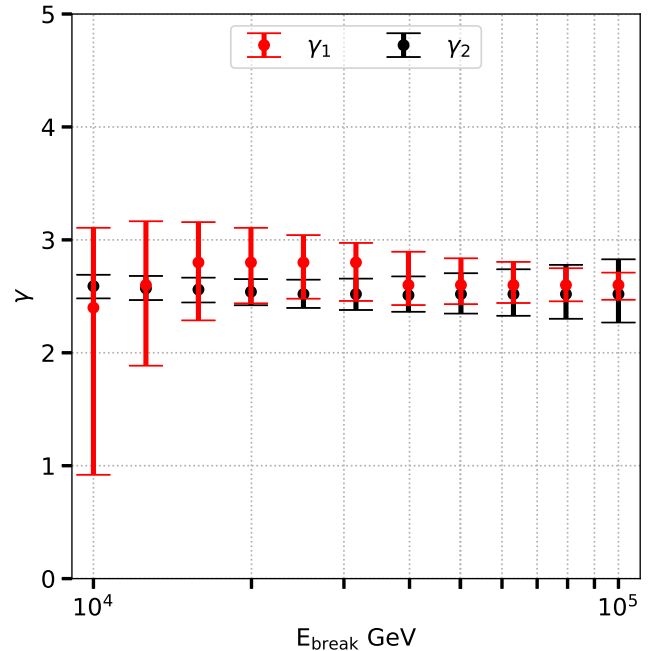

FIG. 12. Best-fit low energy spectral indexes, γ_1, calculated assuming various energy breaks. For each point tested, all parameters are allowed to be refit. We lose sensitivity to harder spectrum as the energy break is decreased. We observe the higher energy spectral index to be stable for various models (in black).

1068, an AGN for which IceCube recently reported evidence of TeV neutrino emission that is not matched by a corresponding gamma-ray signal [22].

D. Measurement of the diffuse flux assuming a nonisotropic diffuse flux

We now treat the astrophysical neutrino flux as a sum of two single power laws, one for each hemisphere where the hemisphere is defined using the IceCube local coordinate system. This model is defined as

$$\Phi_{\text{Astro}}^{\text{Total}}/C_0 = \phi_{\text{Astro},S} \times \left(\frac{E_\nu}{100 \text{ TeV}}\right)^{-\gamma,S} (\Theta_\nu < 90°)$$
$$+ \phi_{\text{Astro},N} \times \left(\frac{E_\nu}{100 \text{ TeV}}\right)^{-\gamma,N} (\Theta_\nu > 90°),$$

where we found:

$$\phi_{\text{per flavor}}^{\text{Astro,North}} = 1.28_{-1.28}^{+0.83}, \qquad \gamma_{\text{North}} = 2.36_{-1.05}^{+0.24},$$
$$\phi_{\text{per-flavor}}^{\text{Astro,South}} = 1.56_{-0.24}^{+0.28}, \qquad \gamma_{\text{South}} = 2.66_{-0.16}^{+0.13}. \quad (9)$$

Given the excellent angular resolution from starting tracks, the hemisphere measurements can be interpreted as independent. The best-fit points and 68% confidence intervals are shown in Fig. 13 as solid blue and red lines in addition to the isotropic SPL measurement in black.
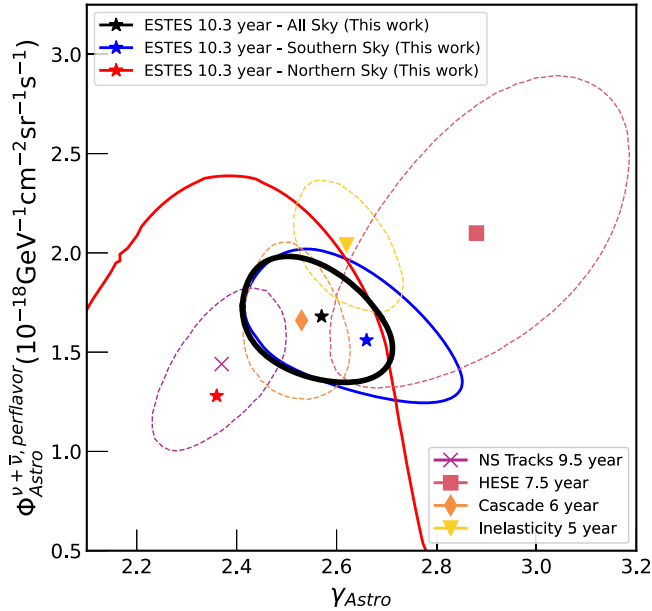

FIG. 13. A summary of the SPL 68% confidence intervals for the All-Sky, Southern-Sky, and Northern-Sky SPL measurements. The IceCube "inelasticity" measurement [53] is shown as yellow dotted lines. It is the only existing measurement of the flux using starting track events; we note the precision is limited due to harsh cuts in the southern sky. We include recent IceCube results for direct comparison [49–51].

We conclude that the fluxes are compatible with each other. It is interesting to see that the southern sky measurement is significantly more constraining—a consequence of the higher proportion of astrophysical neutrinos in the southern sky due to the atmospheric neutrino self-veto.

A smaller, but non-negligible, source of neutrinos from the galactic plane is expected [100–103] below 100 TeV. The Fermi-LAT benchmark model [104,105] describes the diffuse emission of gamma rays likely due to the interaction of cosmic rays with the interstellar medium (ISM) (or surrounding sources). In these interactions, both charged and neutral pions are produced. The neutral pions (π^0) decay into a photon pair while the charged pions ($\pi^\pm$) decay into neutrinos and muons. Therefore, the expected diffuse neutrino flux from the galactic plane is closely connected to gamma ray measurements. This neutrino model is referred to as the Fermi-π^0 model as described in reference [106]. The spatial distribution of the gamma rays is considered and it is further combined with a neutrino single power law flux of $E^{-2.7}$.

We directly test the impact of the galactic plane on the isotropic diffuse flux measurement, treating the Fermi-π^0 flux normalization as a Gaussian nuisance parameter using the measured fluxes from an IceCube dedicated search for neutrinos from the galactic plane [23]. Figure 14 shows the measured isotropic diffuse flux after including the Fermi-π^0 term and fitting to the data again. We observe at most a 10% impact on the isotropic normalization with negligible impact on the spectral index. The same treatment was performed for the segmented flux measurement. The flux normalization shifts are shown in Table IV. This treatment was also repeated for the broken power law measurement VII C and hemisphere measurement VII D with negligible impact. Given the large errors introduced by adding the
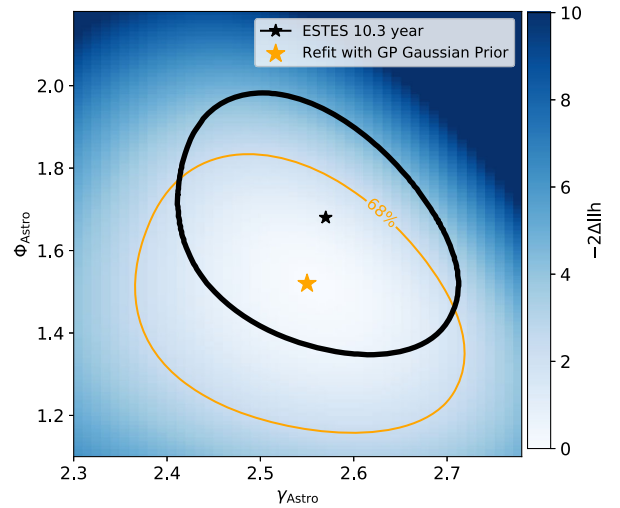

FIG. 14. Single power law flux measurement as described in Sec. VII A (in black) and introducing the galactic plane as additional nuisance parameter in the fit.

TABLE V. Prompt upper limits as computed under the single power law and broken power law flux astrophysical models. We observe similar results with a slightly worse limit for the BPL due to the additional flexibility in the model.

UL $\times \Phi_{prompt}$	90% upper limit
Single Power Law	3.19
Broken Power Law	3.20

galactic plane diffuse model, an extension of this measurement including right ascension is motivated but beyond the scope of this work.

E. Search for prompt atmospheric neutrinos

Atmospheric neutrinos resulting from the decay of charmed mesons in atmospheric showers are referred to as prompt neutrinos. The charmed mesons decay promptly resulting in a harder spectrum than their conventional counterparts. We treat the prompt neutrino flux as an independent parameter with the cosmic ray model and self-veto uncertainties applied as described in Sec. VI B. The assumed cosmic-ray flux model is Gaisser H4a-GST with Sibyll 2.3c. For reference, the theoretical BERSS flux [107] is ~3× smaller at 50 TeV and the ERS flux [108] is similar to the theoretical prompt flux tested here. We do not observe any evidence for the prompt flux and show the test-statistic in Table V. We searched for the prompt flux assuming a single power law and broken power law flux hypothesis from Sec. VI and Sec. VII C, respectively setting limits on the prompt flux under both of these astrophysical flux models. The limits shown correspond to a scaling factor multiplied by the prompt flux shown in Fig. 15.

F. Diffuse flux measurement summary and outlook

Figure 13 shows a summary of all recent IceCube measurements of the astrophysical diffuse flux. Most importantly, it shows that despite numerous techniques employed over the past decade, the different neutrino data sets converge toward similar results.

The HESE 7.5 year measurement [51] focuses on high energy starting events. The dataset is dominated by cascadelike events with a non-negligible contribution from starting tracklike events (17% starting tracks). The HESE analysis applies a minimum energy cut at 60 TeV limiting the measurement of the astrophysical flux to higher energy. This also limits the statistics and correspondingly leads to a measurement that is statistically limited (largest contour in Fig. 13).

The Cascade 6-year and 5-year measurements [49,53] are driven by cascade events extending IceCube's sensitivity to the astrophysical flux down to 16 TeV. These lower energy measurements take advantage of the self-veto effect, assuming a muon response modeled as a fixed step-function. While these measurements are greatly constraining, we now believe that any measurement utilizing the self-veto effect should be inclusive of uncertainties from the choice of self-veto flux model.

The Northern Sky Tracks 9.5-year measurement uses through going and starting muon tracks in the northern equatorial sky ($\theta > 85°$). This measurement is limited by the energy resolution of the through-going events because the reconstructed muon energy can only be interpreted as a lower limit on the expected neutrino energy. The zenith angle cut also means there is no self-veto effect to take advantage of. However, the high statistics and wide energy range of this well studied event selection makes it a powerful measurement.
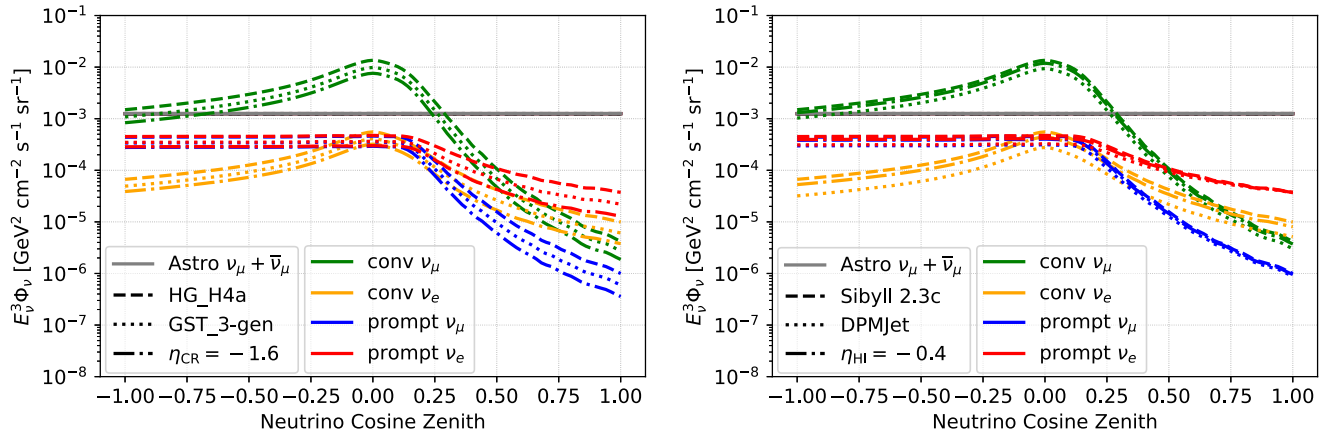

FIG. 15. Conventional and prompt atmospheric neutrino fluxes at 50 TeV shown as a function of cosine zenith for the various choices of cosmic ray models (left) and hadronic interaction models (right). The fluxes labeled as $\eta_{CR/HI}$ are the best-fit interpolated fluxes as defined in Table III. We observe large differences between the theoretical cosmic-ray flux model and the preferred model, but minor differences between the hadronic models and the preferred model. We use the SPL best fit $\eta_{Self\text{-}Veto} = 2.1$ (126 GeV) for the fluxes shown here.

The ESTES 10.3-year measurement (this work) searches for starting tracklike events over the entire sky for energies above 1 TeV. This event selection takes advantage of the excellent energy and directional resolution of such an event morphology. In the southern sky, the self-veto effect improves the astrophysical neutrino purity of the selection.

VIII. CONCLUSION

A measurement of the astrophysical diffuse neutrino flux was presented in this work using novel techniques. This paper outlined the construction of the ESTES dataset, its performance, and the measurement of the diffuse flux from the ESTES selection applied to 10.3 years of IceCube data. We also outlined the new systematic uncertainty terms: self-veto effect and hadronic interaction model gradient which were shown to contribute non-negligible impacts on the astrophysical flux measurement. A search for the atmospheric prompt neutrino flux was also presented. No evidence for the prompt flux was found and upper limits were set on the Gaisser H4a-GST cosmic ray model with Sibyll 2.3c prompt flux model of 3.2 times the theoretical prediction. The amplitude of the prompt flux remains one of the unresolved mysteries in the diffuse neutrino sky.

The ESTES dataset of 10,798 events was extracted using veto-techniques and boosted decision trees to search for starting track events in the northern and southern hemisphere. The overwhelming atmospheric muon background was successfully reduced from 3 kHz down to 1 μHz ($<1\%$ of the remaining data) while retaining a large effective area for neutrinos in the southern hemisphere. The dataset observed at least 10,000 neutrino events of which 1000 were localized to the southern sky. This dataset opens up the possibility of conducting other neutrino studies, such as searching for neutrino sources in the southern sky.

The ESTES dataset was used to search for, and characterize, the astrophysical neutrino flux. Both a single power law and broken power law form for the astrophysical flux were fitted. The best-fit spectral index for the single power law fit is $\gamma = 2.58^{+0.10}_{-0.09}$ and per-flavor normalization is $\Phi^{\text{Astro}}_{\text{per-flavor}} = 1.68^{+0.19}_{-0.22}$ (at 100 TeV). The sensitive energy range for this particular flux model is 3–550 TeV, marking the first time the neutrino flux is measured to such precision below 16 TeV. The observation of the diffuse flux below 100 TeV is in agreement with, and independent from, IceCube's 6-year cascade-event based result [49]. Assuming the single power law flux, we then presented a segmented measurement of the normalization from 300 GeV to 100 PeV showing consistent normalization with the measured single power law.

We tested the impact of the galactic plane under the Fermi π^0 flux model and concluded that while the expected impact on the diffuse flux spectral index is at the subpercent level it can still contribute to the overall normalization by $\sim 10\%$.

Finally, a measurement of the flux under the broken power law assumption was performed. We tested a lower (higher) energy spectral index below (above) a break energy. We are able to reject $\gamma_1 < 1$ to greater than 3σ significance and $\gamma_1 < 2$ to 2.1σ significance for energies below 23 TeV. At 40 TeV, we measure $\gamma_1 = 2.6^{+0.3}_{-0.2}$ which is largely consistent with IceCube's 6-year result using cascades [49]. Overall, we do not observe a departure from a single power law at lower energies.

In conclusion, we present a measurement of the diffuse flux over the entire sky from 300 GeV to 100 PeV using the starting track event morphology. This is the first measurement of starting tracks below 100 TeV, allowing us to study the diffuse astrophysical neutrino flux with a new sample at lower energies. No evidence was found for structure in the flux beyond a single power law spanning from 3 TeV to 550 TeV.

ACKNOWLEDGMENTS

APPENDIX A: BOOSTED DECISION TREE INPUTS

The thirteen variables used in the event selection's boosted decision tree are shown in Table VI sorted by importance after training.

APPENDIX B: ATMOSPHERIC FLUX SYSTEMATICS

The atmospheric neutrinos were modeled using the Gaisser H4a cosmic ray [62] and Sibyll 2.3c hadronic interaction [63] models. We treat the normalization of the conventional and prompt neutrino fluxes (Φ_{conv}, Φ_{prompt}) and the conventional atmospheric muon flux (Φ_{muon}) as nuisance parameters by using overall normalization factors for each component. The $\epsilon_{\nu\bar{\nu}\text{-ratio}}$ systematic uncertainty is centered at 1.0 with a Gaussian prior of 0.10. This ratio term controls the relative contributions from atmospheric neutrinos to anti-neutrinos [$\epsilon_{\nu\bar{\nu}\text{-ratio}} = 2\nu/(\nu + \bar{\nu})$] and is used as a correction term to the theoretical expectation. The choice of 10% is an estimate derived by comparing various

atmospheric flux models [109] and taking the maximal differences. The same ratio term is used for conventional and prompt atmospheric neutrinos.

The $\eta_{\text{H4a--GST}}$ systematic uncertainty was motivated by the expected shape differences between different cosmic ray flux models parametrized in MCEq. This parameter was first introduced in a recent measurement of the flux using tracks from the northern sky [50]. When $\eta_{\text{H4a--GST}} = 0$, the data agrees perfectly with the H4a cosmic ray flux model and when $\eta_{\text{H4a--GST}} = -1$ the data prefers the GST cosmic ray flux model [110]. A linear interpolation in log-space for the difference of the predicted fluxes was used to model this uncertainty. We allowed some flexibility by constraining the predicted flux at ± 2 and modeling the uncertainty as a flat prior. The expected atmospheric neutrino fluxes and the best-fit $\eta_{\text{H4a--GST}}$ flux are shown in Fig. 15. The same $\eta_{\text{H4a--GST}}$ term was used for conventional and prompt atmospheric neutrino fluxes. The $\eta_{\text{2.3c--DPMJet}}$ systematic uncertainty is modeled using the same technique as described for $\eta_{\text{H4a--GST}}$ but this time interpolating between the Sibyll 2.3c and the DPMJet hadronic interaction models [111]. The $\eta_{\text{2.3c--DPMJet}}$ was introduced as an alternative to using Barr parameters as described in [112].

As initially described in Sec. III B, for cosine zenith > 0 both the conventional and prompt atmospheric neutrino fluxes experience an energy, cosine zenith, and depth-dependent suppression due to the self-veto effect. In previous
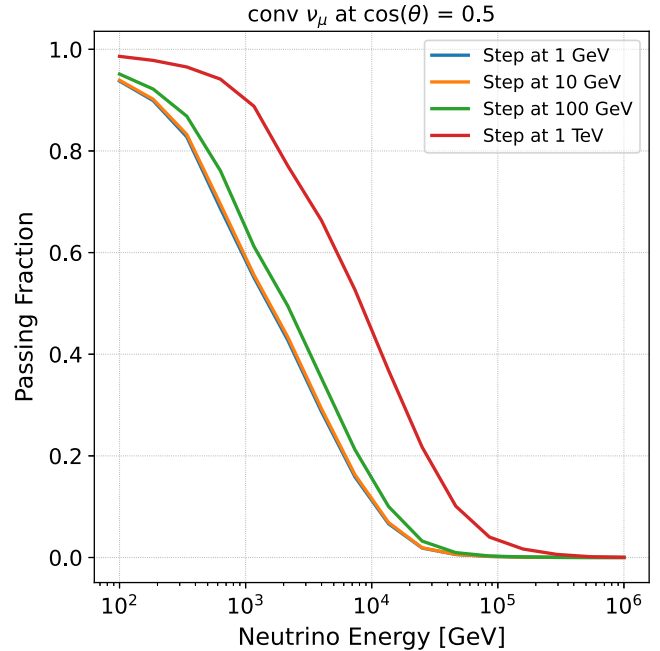
TABLE VI. The 13 BDT inputs sorted by importance after training.

Importance	Description
1	Number of Millipede Losses > 5 GeV
2	Fraction of Energy in First 10 m of Track
3	Max p_{miss} from simple muon hypothesis
4	Classifier
5	Deposited Energy
6	Reconstructed Zenith
7	Fraction of Hits on Outer Layer of Detector
8	Distance to Detector Edge from Perpendicular to Track
9	Distance to Detector Edge from Vertex Position
10	Entry Position of Track—Z position
11	Track Length
12	Fraction of Hits within 100m Cylinder Centered at the Track
13	Max P_{miss} from detailed muon hypothesis

FIG. 16. Conventional atmospheric muon neutrino passing fractions at cosine zenith $= 0.5$. The different colors correspond to different choices of muon energy used for the Heaviside step function. The muon threshold energy is treated as a free parameter in our model.

IceCube cascade-dominated measurements using the southern sky [49,52], it was assumed that muons with energy greater than 1 TeV are all rejected. This rejection probability is defined as a Heaviside step function [54,55]. While the choice of 1 TeV is well motivated (muons are minimum ionizing particles below this energy), it is conservative to treat this energy threshold as a free-parameter in the measurement. The $\eta_{\text{Self-Veto}}$ nuisance parameter is defined as a parameter that weakens and strengthens the muon rejection probability function. The introduction of this nuisance parameter is motivated such that we minimize the potential bias on the flux measurement due to choice of muon rejection probability model. The value corresponds to the muon energy used in a Heaviside function. Different choices of this probability are used to calculate the atmospheric neutrino flux. Figure 16 shows the passing fraction (P_{frac}) which is the ratio of the flux with the self-veto divided by the flux without the self-veto effect. We note there are minor differences at lower muon energies, but for energies above 100 GeV large differences in P_{frac} are expected. We parametrize the $\eta_{\text{Self-Veto}}$ term as a function of the threshold muon energy for each energy-zenith bin used in the measurement. The preferred threshold for this data is 126 GeV as shown in Table III.

APPENDIX C: DETECTOR SYSTEMATICS

Detector uncertainties are defined as any systematic uncertainty that can affect the detector response due to the modeling of the Cherenkov photons in the simulation. These arise due to limited knowledge of the optical properties of the South Pole ice and overall PMT response. The five systematic parameters discussed in Table III are parameterized by rerunning the same set of events through the detector simulation under various ice and detector configurations. A "baseline" simulation set is centered at the mean and then varied within the allowed range to parametrize the detector response per nuisance parameter. Linear interpolation is assumed between the simulated ranges as shown in Table III for each bin in the energy/zenith observable space.

The South Pole bulk-ice refers to the ice between the strings in the detector. A depth-dependent parametrization [72,73] of the photon scattering [113] and absorption [114] coefficients is used in simulations to account for the effect of glacial ice impurities [115,116] and structural properties of the ice, on photon propagation. We model $\epsilon_{\text{Scattering}}$ and $\epsilon_{\text{Absorption}}$ as Gaussian terms centered at nominal scattering/absorption parameters with a $\pm 5\%$ overall uncertainty.

The photomultiplier tube in an IceCube DOM points downward, causing a large zenith angle dependence in the photon detection efficiency [117]. Up-going photons that enter the DOM directly will enter the PMT head-on resulting in maximal photon detection efficiency, whereas down-going photons that enter the DOM need to scatter within the optical module itself or the ice surrounding it.

The columns of refrozen ice containing the DOMs have higher concentrations of impurities, particularly air bubbles [118]. This results in the hole-ice having different optical properties when compared to that of the bulk-ice [57,119]. We model the effects of the hole-ice as a single angular response function using two parameters, $\epsilon_{\text{Angular,DOM}(p_0)}$ and $\epsilon_{\text{Angular,DOM}(p_1)}$ with arbitrary units [120] (parameters hold no physical meaning themselves). These parameters were simulated over the ranges shown in Fig. 17 and treated as independent parameters. The colors represent discrete choices of p_0 and p_1 parameters simulated for the ranges indicated in Table III.

The DOM efficiency uncertainty represents the cumulative systematic error of the absolute sensitivity of the sensor within IceCube [58]. Calibration studies of the absolute sensitivity found differences between the simulated charge and observed charge from 5% to 10% in some regions of the detector [121]. We model the DOM efficiency using a Gaussian constraint term centered at 1.0 with an uncertainty of ± 0.10 as motivated by muon studies ($\epsilon_{\text{Overall,DOM}}$) [77]. This overall scaling factor is applied to all IceCube DOMs.

The detector systematics are treated as uncorrelated parameters in the likelihood. When applicable, a Gaussian penalty term is added to the likelihood to better inform our model of external measurements. The same set of neutrino events as described in Sec. II are propagated through the event selection as described in Sec. V. The energy and
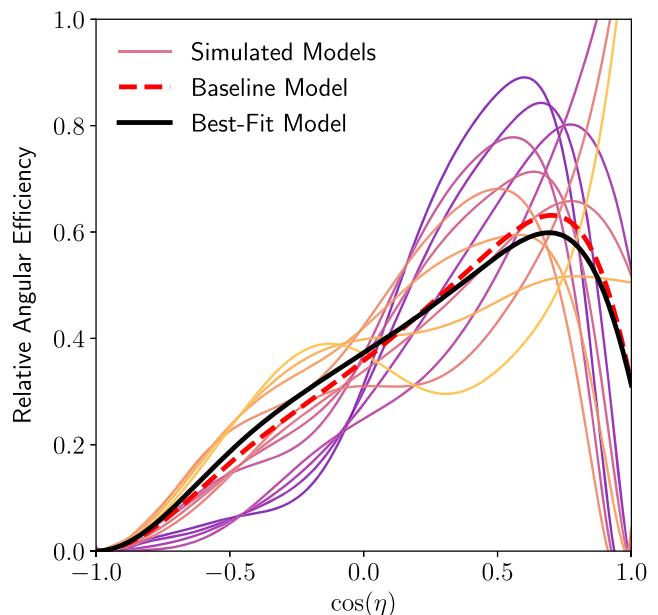

FIG. 17. The optical module angular response function. The discrete colors represent slices of the p_1 and the color gradients represent the range of p_0 simulated. These parameters are modeled as a continuous set of parameters in the likelihood. η is the photon incident angle where $\cos \eta = 1$ is the photon entering upward incident with the PMT.
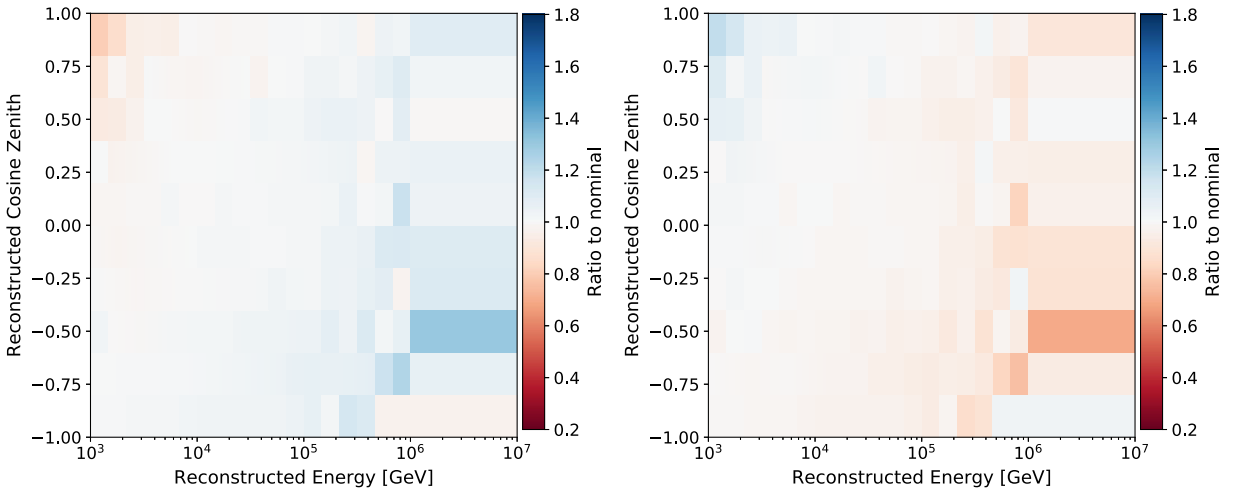
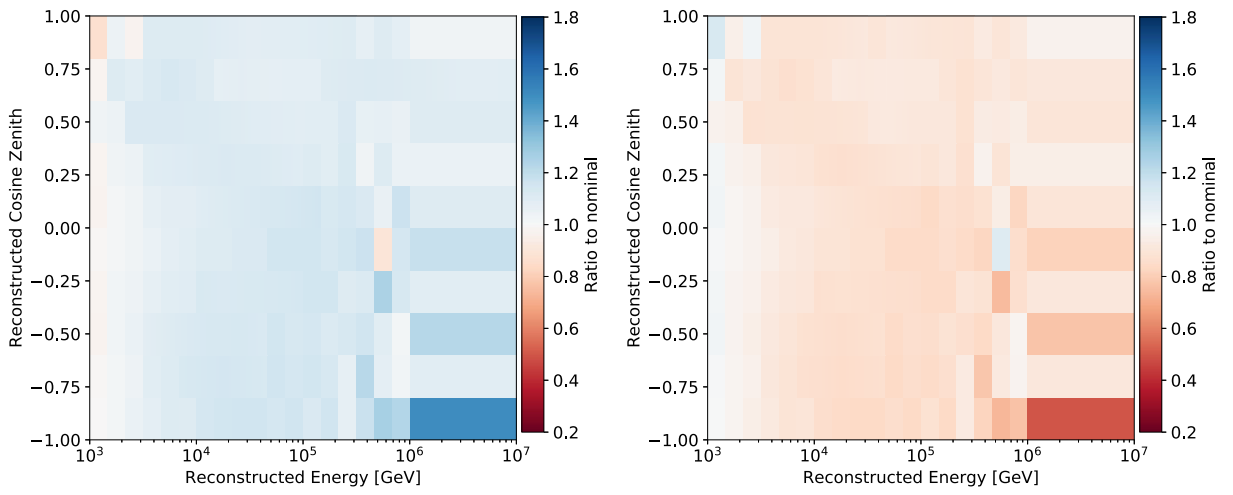FIG. 18.   Scattering coefficients shifted by $+1$ and -1σ.

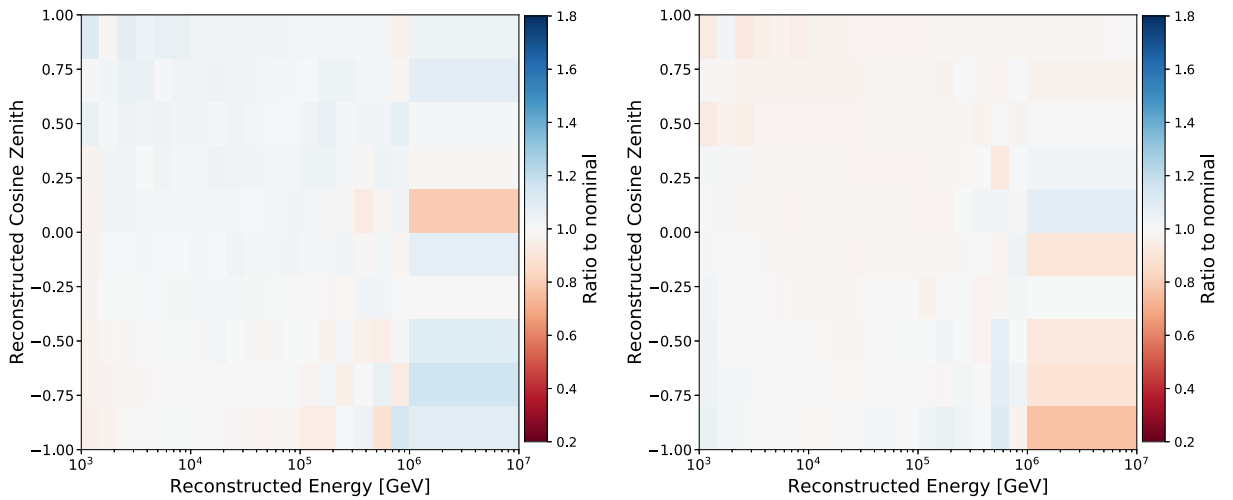FIG. 19.   Absorption coefficients shifted by $+1$ and -1σ.

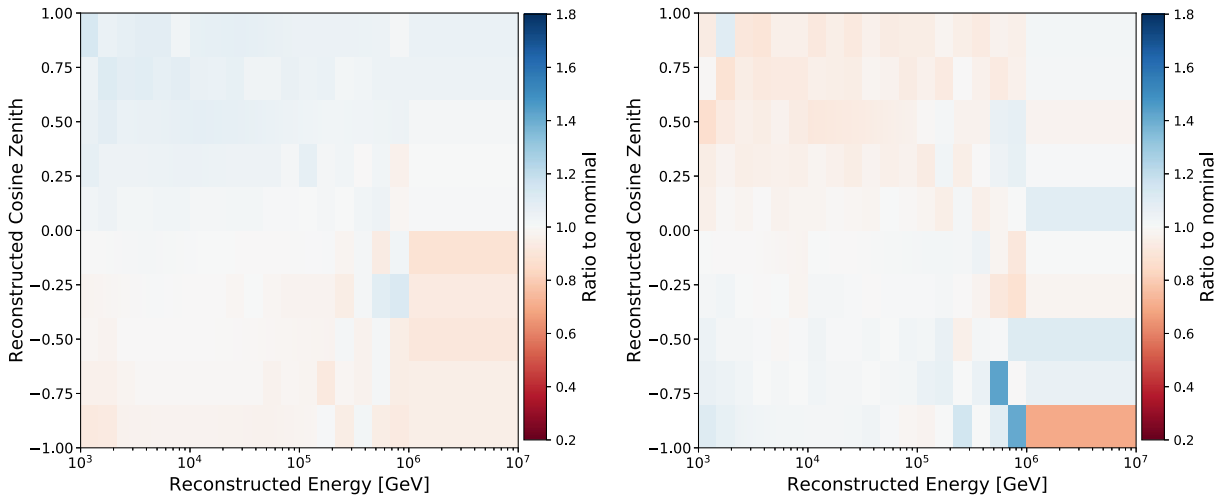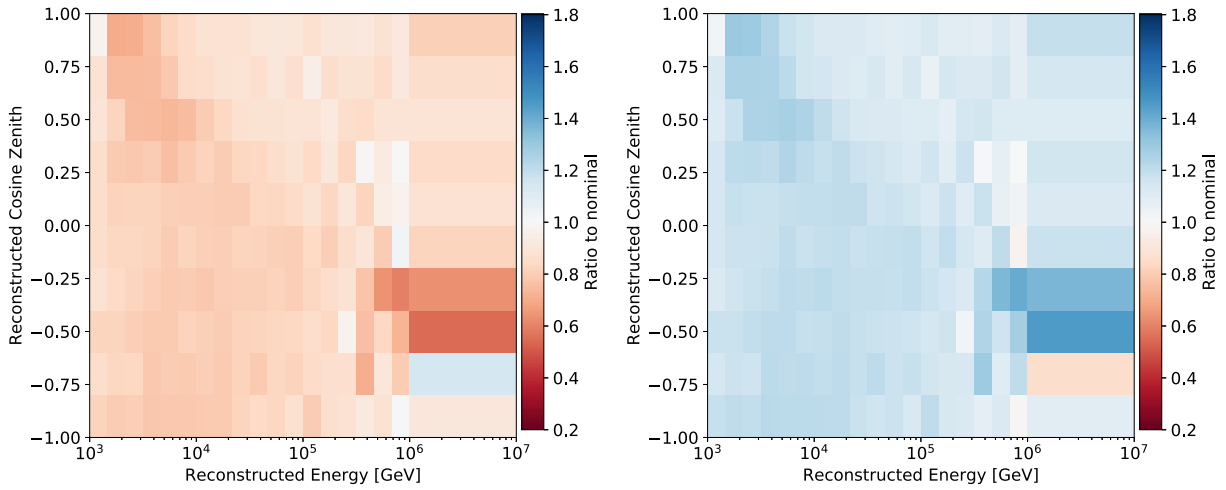FIG. 20.   Hole-ice p_0 parameter shifted by $+1$ and -1σ.

FIG. 21.   Hole-ice p_1 parameter shifted by $+1$ and -1σ.

FIG. 22.   DOM overall efficiency shifted by $+1$ and -1σ.

directional reconstructions are then reevaluated under these new detector configurations. The changes in the detector response are shown as $\pm 1\sigma$ shifts in the event expectation with respect to their nominal expectation in Figs. 18–22. The 2D MC templates are only shown at their $\pm 1\sigma$ point but intermediate points were also simulated such that we construct a 1D parametrization of the detector response per systematic uncertainty.

APPENDIX D: SINGLE POWER LAW VALIDATION

Figure 23 shows the computed pulls on the data over the full 2D observable space. There are no significant deviations observed from our expectation.

The correlation matrix between all physics and nuisance parameters is shown in Fig. 24 computed using the Hessian matrix [122–124]. The spectral index and astrophysical
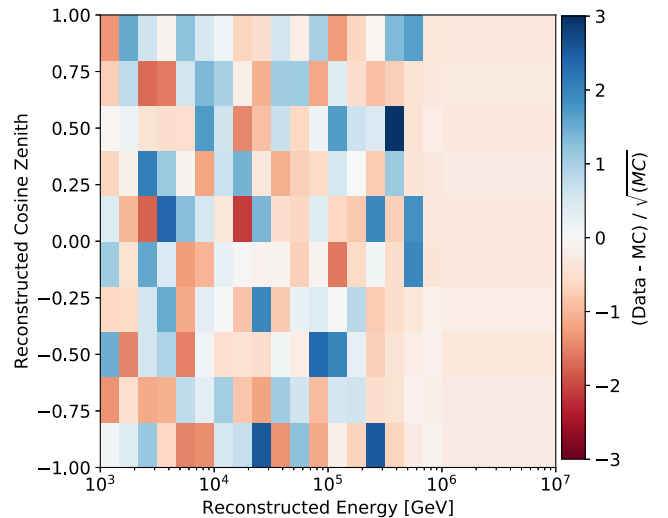

FIG. 23.   The pulls on each energy/zenith bin for the data and Monte Carlo. No unexpected effects are observed.
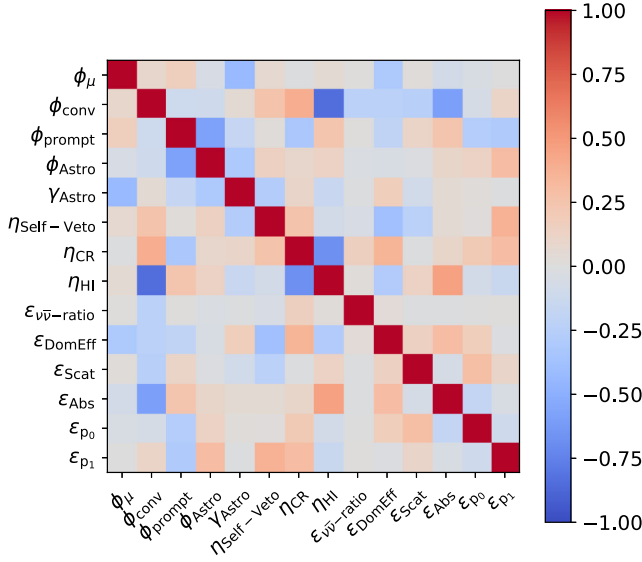
FIG. 24. Correlation matrix for the single power law flux measurement for all parameters used in the likelihood fit. The correlations are computed using the Hessian matrix.

normalization are not correlated or anticorrelated with any particular parameter. The strongest correlation for astrophysical normalization is with the hadronic interaction model uncertainty, whereas the strongest correlation for spectral index is with the atmospheric muon flux.

APPENDIX E: SEGMENTED POWER LAW VALIDATION

Figure 25 shows a check for the stability of each segment over two portions of the sky. In this test, the most vertical bins are removed and the segmented flux is recomputed for the same segments. We note all segments remain consistent despite the reduction in sample size. However, we also note that the 3–10 TeV segment decreased by more than 1σ. We found the most dominant background to astrophysical neutrinos at such energies and zeniths to be from misreconstructed atmospheric neutrinos from the horizon. A full set of figures is found in Appendix F. Future iterations of this analysis should be performed using more robust directional reconstructions to reduce this background.

To directly compare to the segmented power law measurement from the 6-year IceCube cascade result [49], the segmented fit was performed again using the same energy bins. The result is shown in Fig. 26. The tension in the 4.64–10 TeV bin is 2.3σ. The maximum tension per bin is in the 21.5–46.4 TeV bin at 3.7σ (omitting trials correction factor). We observe a "dip"-like structure between 215–464 TeV (similar to that observed with cascades), but note that the reported upper limit is worse despite the improved livetime of this dataset. The larger number of bins leads to increased correlations of up to ±25–30% between bins.
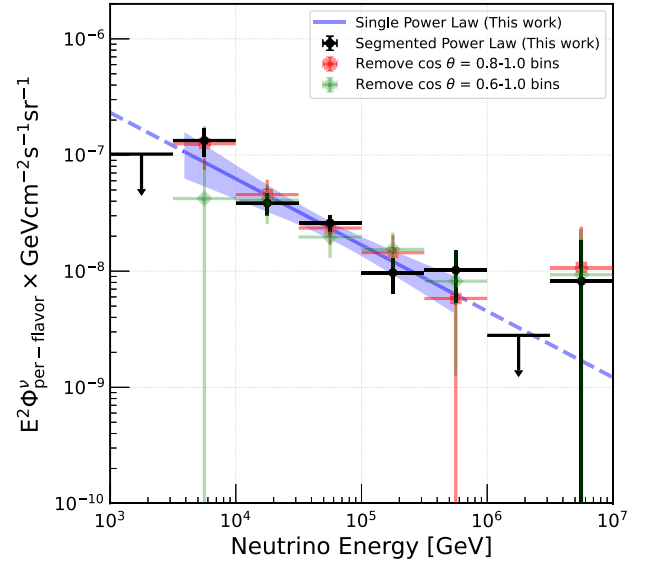

FIG. 25. Distribution of the unfolded flux as first shown in Fig. 11 and the unfolded fluxes after removing the most vertical bins from the measurement. This cross-check was performed to test the isotropic-qualities of all segments. We observe a stable flux over all energies.
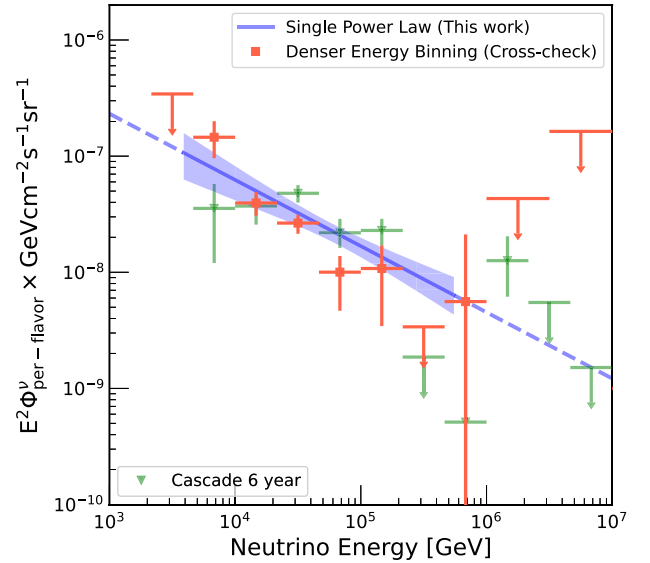
FIG. 26. Distribution of the unfolded flux as first shown in Fig. 11. The red points are the segmented flux measurement using denser energy binning as a cross-check to compare directly with 6-year IceCube cascade result [49]. There is no sensitivity to the astrophysical flux in the 1–2.15 TeV bin.

APPENDIX F: PREDICTED NEUTRINO ZENITHS

The true cosine zenith distributions are shown in Fig. 27. Cuts for each subplot are made on the reconstructed zenith used as an observable in the measurement. The simulated rates take into account the parameters from Table III.
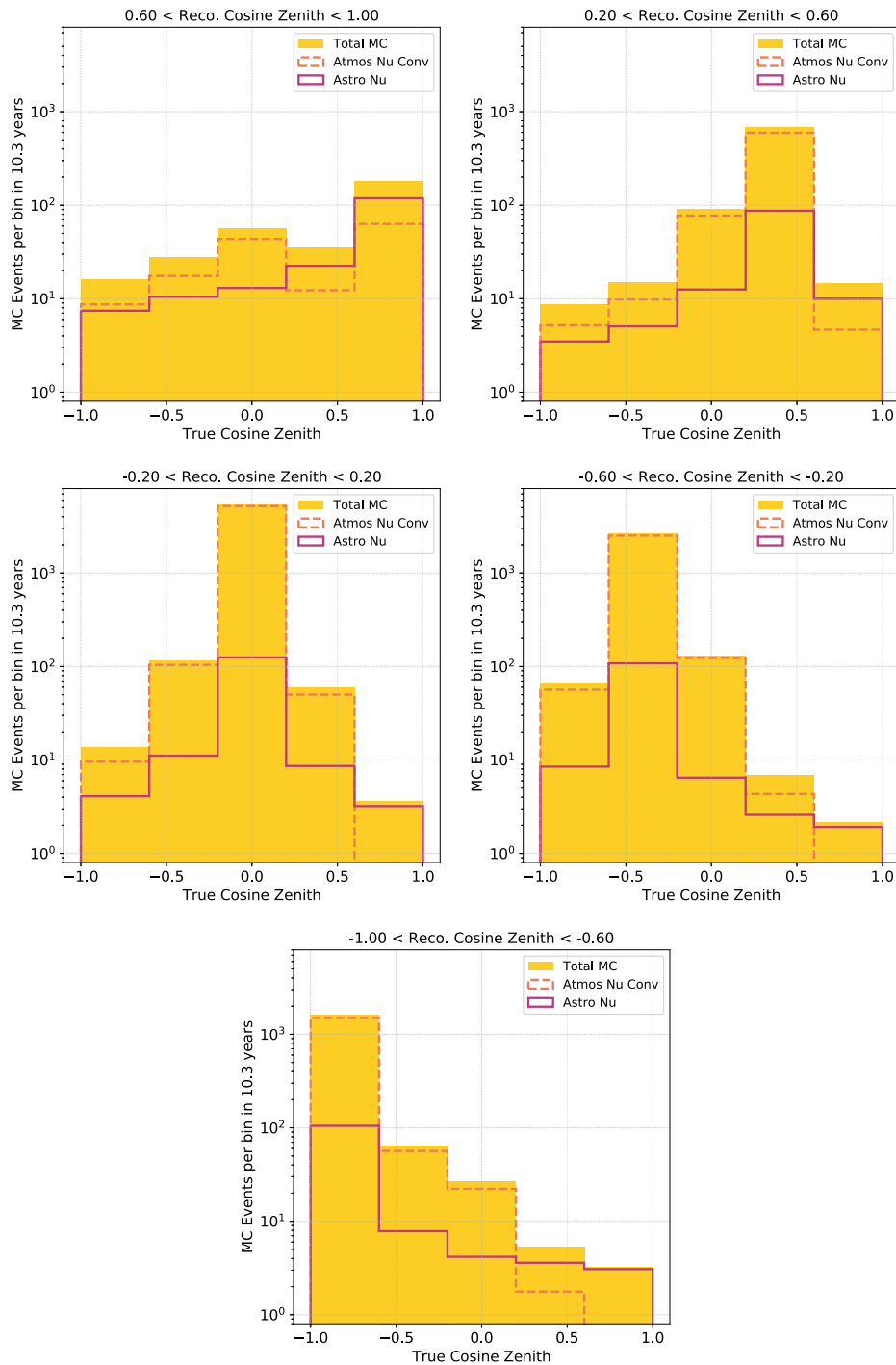
FIG. 27. True cosine zenith distributions using the neutrino simulation. Each subfigure is binned by reconstructed cosine zenith distribution. We draw attention here to the dominant background in reconstructed zenith = 0.6–1.0. These events are determined to be a mixture of true neutral current events and high inelasticity muon neutrinos in the charged current channel. Future iterations of this dataset can improve purity by applying more robust directional reconstructions.

[1] M. G. Aartsen *et al.* (IceCube Collaboration), Science **342,** 1242856 (2013).

[2] M. G. Aartsen *et al.* (IceCube Collaboration), Phys. Rev. Lett. **111,** 021103 (2013).

[3] M. G. Aartsen *et al.* (IceCube Collaboration), Phys. Rev. Lett. **113,** 101101 (2014).

[4] R. L. Workman *et al.* (Particle Data Group), Prog. Theor. Exp. Phys. **2022,** 083C01 (2022).

[5] E. Fermi, Phys. Rev. **75,** 1169 (1949).

[6] G. F. Krymskii, Akad. Nauk SSSR Dokl. **234,** 1306 (1977), https://www.mathnet.ru/php/archive.phtml?wshow=paper& jrnid=dan&paperid=41069&ption_lang=eng.

[7] A. R. Bell, Mon. Not. R. Astron. Soc. **182,** 147 (1978).

[8] J. K. Becker, Phys. Rep. **458,** 173 (2008).

[9] T. Kashti and E. Waxman, Phys. Rev. Lett. **95,** 181101 (2005).

[10] K. Z. Jero, A search for starting tracks in IceCube: A new window for detecting astrophysical neutrinos, Ph.D. thesis, University of Wisconsin, Madison, 2017.

[11] M. Silva and S. Mancina (IceCube Collaboration), Proc. Sci., ICRC2019 (**2020**) 1010.

[12] S. Mancina and M. Silva (IceCube Collaboration), Proc. Sci., ICRC2019 (**2020**) 954.

[13] M. Silva (IceCube Collaboration), J. Instrum. **16,** C09015 (2021).

[14] S. Mancina and M. Silva (IceCube Collaboration), J. Instrum. **16,** C09024 (2021).

[15] R. Abbasi *et al.* (IceCube Collaboration), Proc. Sci., ICRC2021 (**2021**) 1130.

[16] M. Silva, S. Mancina, and J. Osborn (IceCube Collaboration), Proc. Sci., ICRC2023 (**2023**) 1008.

[17] S. L. Mancina, Astrophysical neutrino source searches using IceCube starting tracks, Ph.D. thesis, University of Wisconsin, Madison, 2022.

[18] M. Silva, Measurement of the astrophysical diffuse neutrino flux using starting track events in IceCube, Ph.D. thesis, University of Wisconsin, Madison, 2023.

[19] R. Abbasi *et al.* (IceCube Collaboration) (to be published).

[20] M. G. Aartsen *et al.* (IceCube Collaboration), Science **361,** 147 (2018).

[21] M. G. Aartsen *et al.* (IceCube, Fermi-LAT, MAGIC, AGILE, ASAS-SN, HAWC, H.E.S.S., INTEGRAL, Kanata, Kiso, Kapteyn, Liverpool Telescope, Subaru, Swift NuSTAR, VERITAS, VLA/17B-403 Collaborations), Science **361,** eaat1378 (2018).

[22] R. Abbasi *et al.* (IceCube Collaboration), Science **378,** 538 (2022).

[23] R. Abbasi *et al.* (IceCube Collaboration), Science **380,** 1338 (2023).

[24] K. Murase and E. Waxman, Phys. Rev. D **94,** 103006 (2016).

[25] F. Capel, D. J. Mortlock, and C. Finley, Phys. Rev. D **101,** 123017 (2020).

[26] R. Abbasi *et al.* (IceCube Collaboration), Astrophys. J. **951,** 45 (2023).

[27] K. Fang, J. S. Gallagher, and F. Halzen, Astrophys. J. **933,** 190 (2022).

[28] K. Murase, D. Guetta, and M. Ahlers, Phys. Rev. Lett. **116,** 071101 (2016).

[29] A. Loeb and E. Waxman, J. Cosmol. Astropart. Phys. 05 (2006) 003.

[30] K. Murase, S. Inoue, and S. Nagataki, Astrophys. J. Lett. **689,** L105 (2008).

[31] V. S. Berezinsky and A. A. Mikhailov, in *Possible Regions of Origin of Ultrahigh Energy Cosmic Rays in Our Galaxy*, International Cosmic Ray Conference, Moscow, USSR Vol. 2 (1987), p. 54, https://cds.cern.ch/record/867657? ln=en.

[32] D. Eichler, Astrophys. J. **232,** 106 (1979).

[33] D. Kazanas and D. C. Ellison, Astrophys. J. **304,** 178 (1986).

[34] M. C. Begelman, B. Rudak, and M. Sikora, Astrophys. J. **362,** 38 (1990).

[35] F. Haardt and L. Maraschi, Astrophys. J. Lett. **380,** L51 (1991).

[36] F. W. Stecker, C. Done, M. H. Salamon, and P. Sommers, Phys. Rev. Lett. **69,** 2738 (1992).

[37] A. P. Szabo and R. J. Protheroe, Astropart. Phys. **2,** 375 (1994).

[38] J. Alvarez-Muniz and P. Meszaros, Phys. Rev. D **70,** 123001 (2004).

[39] A. Cuoco and S. Hannestad, Phys. Rev. D **78,** 023007 (2008).

[40] H. B. J. Koers and P. Tinyakov, Phys. Rev. D **78,** 083009 (2008).

[41] I. B. Jacobsen, K. Wu, A. Y. L. On, and C. J. Saxton, Mon. Not. R. Astron. Soc. **451,** 3649 (2015).

[42] K. Murase, in *Neutrino Astronomy: Current Status, Future Prospects*, edited by T. Gaisser and A. Karle (World Scientific Publishing, Singapore, 2017), pp. 15–31.

[43] S. Razzaque, P. Mészáros, and E. Waxman, Phys. Rev. Lett. **93,** 181101 (2004).

[44] S. Ando and J. F. Beacom, Phys. Rev. Lett. **95,** 061103 (2005).

[45] H. B. J. Koers and R. A. M. J. Wijers, arXiv:0711.4791.

[46] S. R. Klein, R. E. Mikkelsen, and J. Becker Tjus, Astrophys. J. **779,** 106 (2013).

[47] K. Murase, M. Ahlers, and B. C. Lacki, Phys. Rev. D **88,** 121301 (2013).

[48] M. Aartsen *et al.* (IceCube Collaboration), Astropart. Phys. **78,** 1 (2016).

[49] M. G. Aartsen *et al.* (IceCube Collaboration), Phys. Rev. Lett. **125,** 121104 (2020).

[50] R. Abbasi *et al.* (IceCube Collaboration), Astrophys. J. **928,** 50 (2022).

[51] R. Abbasi *et al.* (IceCube Collaboration), Phys. Rev. D **104,** 022002 (2021).

[52] M. G. Aartsen *et al.* (IceCube Collaboration), Phys. Rev. D **91,** 022001 (2015).

[53] M. G. Aartsen *et al.* (IceCube Collaboration), Phys. Rev. D **99,** 032004 (2019).

[54] S. Schönert, T. K. Gaisser, E. Resconi, and O. Schulz, Phys. Rev. D **79,** 043009 (2009).

[55] T. K. Gaisser, K. Jero, A. Karle, and J. van Santen, Phys. Rev. D **90,** 023009 (2014).

[56] C. A. Argüelles, S. Palomares-Ruiz, A. Schneider, L. Wille, and T. Yuan, J. Cosmol. Astropart. Phys. 07 (2018) 047.

[57] M. G. Aartsen *et al.* (IceCube Collaboration), J. Instrum. **12,** P03012 (2017).

[58] R. Abbasi *et al.* (IceCube Collaboration), Nucl. Instrum. Methods Phys. Res., Sect. A **618,** 139 (2010).

[59] R. Abbasi *et al.* (IceCube Collaboration), Nucl. Instrum. Methods Phys. Res., Sect. A **601**, 294 (2009).

[60] P. A. Cherenkov, Dokl. Akad. Nauk SSSR **2**, 451 (1934).

[61] R. Abbasi *et al.* (IceCube Collaboration), Astropart. Phys. **35**, 615 (2012).

[62] T. K. Gaisser, T. Stanev, and S. Tilav, Front. Phys. **8**, 748 (2013).

[63] A. Fedynitch, F. Riehn, R. Engel, T. K. Gaisser, and T. Stanev, Phys. Rev. D **100**, 103018 (2019).

[64] A. Fedynitch, R. Engel, T. K. Gaisser, F. Riehn, and T. Stanev, EPJ Web Conf. **99**, 08001 (2015).

[65] A. Cooper-Sarkar, P. Mertsch, and S. Sarkar, J. High Energy Phys. 08 (2011) 042.

[66] A. M. Dziewonski and D. L. Anderson, Phys. Earth Planet. Inter. **25**, 297 (1981).

[67] A. Gazizov and M. Kowalski, Comput. Phys. Commun. **172**, 203 (2005).

[68] J. van Santen, Neutrino interactions in IceCube above 1 TeV constraints on atmospheric charmed-meson production and investigation of the astrophysical neutrino flux with 2 years of IceCube data taken 2010–2012, Ph.D. thesis, University of Wisconsin, Madison, 2014.

[69] D. Heck, J. Knapp, J. N. Capdevielle, G. Schatz, and T. Thouw, CORSIKA: A Monte Carlo code to simulate extensive air showers, Karlsruhe Institute of Technology, Technical Report FZKA-6019, 1998.

[70] J. H. Koehne, K. Frantzen, M. Schmitz, T. Fuchs, W. Rhode, D. Chirkin, and J. Becker Tjus, Comput. Phys. Commun. **184**, 2070 (2013).

[71] M. P. Kowalski, Search for neutrino-induced cascades with the AMANDA-II detector, Ph.D. thesis, Humboldt-Universität zu Berlin, Mathematisch-Naturwissenschaftliche Fakultät I, 2004.

[72] M. Ackermann *et al.*, J. Geophys. Res. **111** (2006).

[73] M. G. Aartsen *et al.* (IceCube Collaboration), Nucl. Instrum. Methods Phys. Res., Sect. A **711**, 73 (2013).

[74] V. J. Stenger, in Track fitting for dumand-II Octagon Array, Technical Report, University of Hawaii at Manoa, 1990.

[75] M. G. Aartsen *et al.* (IceCube Collaboration), Nucl. Instrum. Methods Phys. Res., Sect. A **736**, 143 (2014).

[76] J. Ahrens *et al.*, Nucl. Instrum. Methods Phys. Res., Sect. A **524**, 169 (2004).

[77] M. G. Aartsen *et al.* (IceCube Collaboration), J. Instrum. **9**, P03009 (2014).

[78] L. Breiman, Mach. Learn. **45**, 5 (2001).

[79] P. Geurts, D. Ernst, and L. Wehenkel, Mach. Learn. **63**, 3 (2006).

[80] R. Abbasi *et al.* (IceCube Collaboration), Nucl. Instrum. Methods Phys. Res., Sect. A **703**, 190 (2013).

[81] M. G. Aartsen *et al.* (IceCube Collaboration), Phys. Rev. Lett. **124**, 051103 (2020).

[82] M. G. Aartsen *et al.* (IceCube Collaboration), J. Instrum. **15**, P06032 (2020).

[83] M. Ackermann *et al.* (IceCube Collaboration), in *30th International Cosmic Ray Conference* (2007).

[84] T. Chen and C. Guestrin, in *Proceedings of the 22nd ACM SIGKDD International Conference on Knowledge Discovery and Data Mining, San Francisco*, KDD '16 (ACM, New York, NY, USA, 2016), pp. 785–794, 10.1145/2939672.2939785.

[85] J. Davis and M. Goadrich, in *Proceedings of the 23rd International Conference on Machine Learning*, ICML '06 (Association for Computing Machinery, New York, NY, USA, 2006), p. 233–240.

[86] F. James and M. Roos, Comput. Phys. Commun. **10**, 343 (1975).

[87] H. Dembinski *et al.*, scikit-hep/iminuit: v2.17.0, Zenodo (2022).

[88] S. S. Wilks, Ann. Math. Stat. **9**, 60 (1938).

[89] S. Baker and R. D. Cousins, Nucl. Instrum. Methods Phys. Res., Sect. A **221**, 437 (1984).

[90] S. Schoenen, Discovery and characterization of a diffuse astrophysical muon neutrino flux with the iceCube neutrino observatory, Dissertation, RWTH Aachen University, Aachen (2017), veröffentlicht auf dem Publikationsserver der RWTH Aachen University; Dissertation, RWTH Aachen University, 2017.

[91] S. L. Glashow, Phys. Rev. **118**, 316 (1960).

[92] M. G. Aartsen *et al.* (IceCube Collaboration), Nature (London) **591**, 220 (2021); **592**, E11 (2021).

[93] A. Bhattacharya, R. Gandhi, W. Rodejohann, and A. Watanabe, J. Cosmol. Astropart. Phys. 10 (2011) 017.

[94] A. Domínguez *et al.*, Mon. Not. R. Astron. Soc. **410**, 2556 (2011).

[95] T. K. Gaisser, *Cosmic Rays and Particle Physics* (Cambridge University Press, Cambridge, England, 1990).

[96] K. Fang, B. D. Metzger, I. Vurm, E. Aydi, and L. Chomiuk, Astrophys. J. **904**, 4 (2020).

[97] M. Ackermann *et al.* (Fermi-LAT Collaboration), Astrophys. J. **799**, 86 (2015).

[98] M. Ackermann *et al.* (Fermi-LAT Collaboration), Phys. Rev. Lett. **116**, 151105 (2016).

[99] A. Capanema, A. Esmaili, and P. D. Serpico, J. Cosmol. Astropart. Phys. 02 (2021) 037.

[100] D. Gaggero, D. Grasso, A. Marinelli, A. Urbano, and M. Valli, Astrophys. J. Lett. **815**, L25 (2015).

[101] A. Albert *et al.*, Astrophys. J. Lett. **868**, L20 (2018).

[102] M. G. Aartsen *et al.* (IceCube Collaboration), Astrophys. J. **849**, 67 (2017).

[103] M. G. Aartsen *et al.* (IceCube Collaboration), Astrophys. J. **886**, 12 (2019).

[104] M. Ackermann *et al.*, Astrophys. J. Suppl. Ser. **203**, 4 (2012).

[105] M. Ackermann *et al.*, Astrophys. J. **750**, 3 (2012).

[106] M. G. Aartsen *et al.* (IceCube Collaboration), Astrophys. J. **849**, 67 (2017).

[107] A. Bhattacharya, R. Enberg, Y. S. Jeong, C. S. Kim, M. H. Reno, I. Sarcevic, and A. Stasto, J. High Energy Phys. 11 (2016) 167.

[108] R. Enberg, M. H. Reno, and I. Sarcevic, Phys. Rev. D **78**, 043005 (2008).

[109] G. Collin, An estimation of systematics for up-going atmospheric muon neutrino flux at the south pole., MIT Libraries: DSpace@MIT (2015), dataset release, https://dspace.mit.edu/handle/1721.1/98078.

[110] T. K. Gaisser, T. Stanev, and S. Tilav, Front. Phys. **8**, 748 (2013).

[111] A. Fedynitch, Cascade equations and hadronic interactions at very high energies, Ph.D. thesis, KIT, Karlsruhe, Dept. Phys., 2015.

[112] G. D. Barr, S. Robbins, T. K. Gaisser, and T. Stanev, Phys. Rev. D **74**, 094009 (2006).

[113] P. Askebjer *et al.*, Appl. Opt. **36**, 4168 (1997).

[114] P. B. Price and L. Bergström, Appl. Opt. **36**, 4181 (1997).

[115] P. B. Price, K. Woschnagg, and D. Chirkin, Geophys. Res. Lett. **27**, 2129 (2000).

[116] M. G. Aartsen *et al.* (IceCube Collaboration), J. Glaciol. **59**, 1117 (2013).

[117] R. Abbasi *et al.* (IceCube Collaboration), Phys. Rev. D **79**, 062001 (2009).

[118] M. Rongen, EPJ Web Conf. **116**, 06011 (2016).

[119] S. Fiedlschuster, The effect of hole ice on the propagation and detection of light in IceCube, Ph.D. thesis, Friedrich-Alexander-Universität Erlangen-Nürnberg, 2019.

[120] R. Abbasi *et al.* (IceCube Collaboration), Phys. Rev. D **108**, 012014 (2023).

[121] D. Tosi and C. Wendt (IceCube Collaboration), Proc. Sci., TIPP2014 (**2014**) 157.

[122] J. C. Spall, J. Comput. Graph. Stat. **14**, 889 (2005).

[123] J. C. Spall, in *2008 American Control Conference* (2008), pp. 2395–2400, 10.1109/ACC.2008.4586850.

[124] S. Das, J. C. Spall, and R. Ghanem, Computational Statistics and Data Analysis **54**, 272 (2010).